

BOUNDARY ELEMENT FORMULATION AND ITS SOLUTION IN  
FORWARD PROBLEM OF ELECTROCARDIOGRAPHY BY USING A  
REALISTIC TORSO MODEL

ARDA KURT

April 2006

BOUNDARY ELEMENT FORMULATION AND ITS SOLUTION IN  
FORWARD PROBLEM OF ELECTROCARDIOGRAPHY BY USING A  
REALISTIC TORSO MODEL

A THESIS SUBMITTED TO  
THE GRADUATE SCHOOL OF APPLIED MATHEMATICS  
OF  
THE MIDDLE EAST TECHNICAL UNIVERSITY

BY

ARDA KURT

IN PARTIAL FULFILLMENT OF THE REQUIREMENTS FOR THE  
DEGREE OF  
MASTER OF SCIENCE  
IN  
THE DEPARTMENT OF SCIENTIFIC COMPUTING

April 2006

Approval of the Graduate School of Applied Mathematics

---

Prof. Dr. Ersan Akyıldız  
Director

I certify that this thesis satisfies all the requirements as a thesis for the degree of Master of Science.

---

Prof. Dr. Bülent Karasözen  
Head of Department

This is to certify that we have read this thesis and that in our opinion it is fully adequate, in scope and quality, as a thesis for the degree of Master of Science.

---

Prof. Dr. Gerhard Wilhelm Weber  
Supervisor

Examining Committee Members

Prof. Dr. Bülent Karasözen

---

Prof. Dr. Gerhard Wilhelm Weber

---

Prof. Dr. Nevzat Güneri Gençer

---

Assist. Prof. Dr. Yeşim Serinağaoğlu Doğrusöz

---

Assist. Prof. Dr. Hakan Öktem

---

I hereby declare that all information in this document has been obtained and presented in accordance with academic rules and ethical conduct. I also declare that, as required by these rules and conduct, I have fully cited and referenced all material and results that are not original to this work.

Name, Last name: Arda Kurt

Signature:

# ABSTRACT

## BOUNDARY ELEMENT FORMULATION AND ITS SOLUTION IN FORWARD PROBLEM OF ELECTROCARDIOGRAPHY BY USING A REALISTIC TORSO MODEL

Arda Kurt

M.Sc., Department of Scientific Computing

Supervisor: Prof. Dr. Gerhard Wilhelm Weber

April 2006, 74 pages

The electrical currents generated in the heart propagate to the outward direction of the body by means of conductive tissues and these currents yield a potential distribution on the body surface. This potential distribution is recorded and analyzed by a tool called electrocardiogram. It is not a problem, if this process continues normally; however, when it is distorted by some abnormalities, the results will be fatal. Electrocardiography (ECG) is the technique dealing with the acquisition and interpretation of the electrical potentials recorded at the body surface due to the electrical activity of the heart. This can be realized by using one of the two approaches utilized in ECG namely; forward and inverse problems. The former one entails the calculation potentials on the body surface from known electrical activity of the heart and the latter one does the reverse. In this thesis, we will construct the body surface potentials in a realistic torso model starting from the epicardial potentials. In order to solve the forward

problem, one needs a geometric model that includes the torso and the heart surfaces, as well as the intermediate surfaces or the intervening volume, and some assumptions about the electrical conductivity inside the enclosed volume. A realistic torso model has a complex geometry and this complexity makes it impossible to solve the forward problem analytically. In this study, Boundary Element Method (BEM) will be applied to solve the forward problem numerically. Furthermore, the effect of torso inhomogeneities such as lungs, muscles and skin to the body surface potentials will be analyzed numerically.

Keywords: Forward problem, boundary element method, realistic torso model.

# ÖZ

## GERÇEKÇİ GÖVDE MODELİ KULLANARAK SINIRLI ELEMEN YÖNTEMİ İLE ELEKTROKARDİYOGRAFİDE İLERİ PROBLEM ÇÖZÜMÜ

Arda Kurt Yüksek Lisans, Bilimsel Hesaplama.  
Tez Yöneticisi: Prof. Dr. Gerhard Wilhelm Weber

Nisan 2006, 74 sayfa

Elektrokardiyografide ileri problem araştırmasının temel nedeni, kalbin bilinen elektriksel aktivitesinden faydalanarak vücut yüzeyindeki elektriksel potansiyeli hesaplamaktır. Bu çalışmada, giriş cümlesinden de anlaşıldığı üzere, kalbin elektriksel aktivitesinin gerçekçi bir gövde modeli üzerindeki elektriksel potansiyeli yapılandırılacaktır. Bu ileri problemi çözmek için, hem kalbi hem de gövdeyi kapsayan geometrik bir modele ihtiyaç olduğu gibi, bu iki yapının arasında bulunan yüzeyler ve bu yüzeylerin elektriksel iletkenlikleri hakkında bazı varsayımlara da gereksinim duyulmaktadır. Gerçekçi bir gövde modelinin karmaşık bir geometriye sahip olması, ileri problemin analitik olarak çözümünü güç kıldığı için Sınır Eleman Yöntemi (BEM) kullanarak bu problemin sayısal çözümü yapılacaktır. Ayrıca, vücudun homojen olmayan, akciğerler, kaslar ve deri tabakası gibi yapılarının vücut yüzeyinde oluşan elektriksel potansiyele etkileri de tartışılacaktır.

Anahtar Kelimeler: İleri problem, sınırlı eleman yöntemi.

To my family

# ACKNOWLEDGMENTS

I would like to thank all those people who have helped in the preparation of this study. I am grateful to Prof. Dr. Gerhard Wilhelm Weber (Willi) for his motivation and support that provided me determination and power throughout this study.

Special thanks to my co-advisor Assist. Prof. Dr. Yeşim Serinağaoğlu Doğrusöz for her support and kindness.

I would also like to thank Prof. Dr. Bülent Karasözen, Prof. Dr. Nevzat Güneri Gençer and Assist. Prof. Dr. Hakan Öktem for their valuable support and time they spared for me.

And, I am grateful with my family so that I dedicated this study to them.

I am indebted to all of my friends, Lerzan, Mert, Emre, Ufuk, Tamer, Turan for their patience and toleration to me during those hard days.

Thank you...

# TABLE OF CONTENTS

|                         |      |
|-------------------------|------|
| PLAGIARISM .....        | iii  |
| ABSTRACT .....          | iv   |
| Öz .....                | vi   |
| ACKNOWLEDGMENTS .....   | viii |
| TABLE OF CONTENTS ..... | ix   |
| LIST OF TABLES .....    | xii  |
| LIST OF FIGURES .....   | xiv  |
| CHAPTER                 |      |
| 1 INTRODUCTION .....    | 1    |
| 1.1 Motivation .....    | 1    |
| 1.2 Purpose .....       | 2    |
| 1.3 Scope .....         | 2    |

|          |  |           |
|----------|--|-----------|
| <b>2</b> | <b>BACKGROUND</b>  | <b>3</b>  |
| 2.1      | The Heart  | 3         |
| 2.1.1    | Anatomy of the Heart   | 3         |
| 2.1.2    | Mechanical Activity of the Heart                             | 3         |
| 2.1.3    | Electrophysiology of the Heart                               | 5         |
| 2.2      | Forward and Inverse Problems of Electrocardiography          | 9         |
| 2.2.1    | Methods in the Forward Problem of ECG                        | 12        |
| 2.3      | Forward Problem and BEM in the Literature                    | 14        |
| 2.3.1    | Different Models   | 14        |
| 2.3.2    | Different Approaches   | 16        |
| <b>3</b> | <b>NUMERICAL SOLUTIONS</b>                                   | <b>17</b> |
| 3.1      | Numerical Solution for the Homogeneous Isotropic Torso Model | 17        |
| 3.1.1    | Motivation of the Method                                     | 17        |
| 3.1.2    | The Model  | 19        |
| 3.1.3    | The Method of Solution                                       | 20        |
| 3.2      | Numerical Solution for the Inhomogeneous Torso Model         | 22        |
| 3.2.1    | Motivation of the Method                                     | 23        |
| 3.2.2    | The Model  | 24        |
| 3.2.3    | The Method of Solution                                       | 24        |
| <b>4</b> | <b>RESULTS AND DISCUSSION</b>                                | <b>27</b> |
| 4.1      | Method of Validation   | 27        |
| 4.2      | Validation of the Numerical Method                           | 29        |

|            |  |    |
|------------|--|----|
| 4.3        | Numerical Solution for Realistic Models . . . . .                  | 35 |
| 4.4        | Examining the Intermediate Matrices . . . . .                      | 43 |
| 5          | SUMMARY AND CONCLUSION . . . . .                                   | 48 |
|            | REFERENCES . . . . .   | 50 |
| APPENDICES |  |    |
| A.1:       | Analytical Derivations for the Homogeneous Torso Model . . . . .   | 58 |
| A.2:       | Analytical Derivations for the Inhomogeneous Torso Model . . . . . | 63 |
| A.3:       | Calculation of the Solid Angle . . . . .                           | 67 |
| A.4:       | Integration over a Plane Triangle . . . . .                        | 69 |
| A.5:       | Inverse Problems . . . . .   | 72 |

# LIST OF TABLES

|      |  |    |
|------|--|----|
| 4.1  | The dipole locations and orientations used in the computations:<br>The values presented are in arbitrary units. . . . .                | 30 |
| 4.2  | Spherical models used in the computations: The values are in<br>arbitrary units. . . . .   | 30 |
| 4.3  | Potential values of some points on the outermost surface calcu-<br>lated by analytical and numerical methods based on Model $M_{21}$ . | 31 |
| 4.4  | RMSE and RDME values for the potential values calculated by<br>analytical and numerical methods based on Model $M_{22}$ . . . . .      | 32 |
| 4.5  | RMSE and RDME values for the potential values calculated by<br>analytical and numerical methods based on Model $M_{23}$ . . . . .      | 32 |
| 4.6  | RMSE and RDME values for the potential values calculated by<br>analytical and numerical methods based on Model $M_{31}$ . . . . .      | 33 |
| 4.7  | RMSE and RDME values for the potential values calculated by<br>analytical and numerical methods based on Model $M_{32}$ . . . . .      | 34 |
| 4.8  | RMSE and RDME values for the potential values calculated by<br>analytical and numerical methods based on Model $M_{33}$ . . . . .      | 34 |
| 4.9  | RMSE and RDME values for the potential values calculated by<br>analytical and numerical methods based on Model $M_{41}$ . . . . .      | 34 |
| 4.10 | RMSE and RDME values for the potential values calculated by<br>analytical and numerical methods based on Model $M_{42}$ . . . . .      | 35 |
| 4.11 | Realistic models used in the computations: The values are in<br>arbitrary units. . . . .   | 37 |

|  |    |
|--|----|
| 4.12 The RDM* values for realistic models. . . . . | 43 |
|--|----|

# LIST OF FIGURES

|     |  |    |
|-----|--|----|
| 2.1 | Location of the heart [8]. . . . .   | 4  |
| 2.2 | Anatomy of the heart [8]. . . . .  | 4  |
| 2.3 | Electrical activity of the heart [8]. . . . .  | 6  |
| 2.4 | A schematic of an electrophysiological recording of an action potential showing the various phases which occur as the wave passes a point on a cell membrane [56]. . . . . | 7  |
| 2.5 | Electrocardiogram signal [57]. . . . .   | 8  |
| 2.6 | Schematic representation of the forward and inverse problem. . .   | 10 |
| 2.7 | Geometric description of the volume conductor. . . . .   | 11 |
| 2.8 | Eccentric spheres model [44]. . . . .  | 15 |
| 3.1 | Homogeneous heart-torso model [7]. . . . .   | 19 |
| 3.2 | Diagrammatic surface used for considering how to construct coefficient matrices $P$ and $G$ [7]. . . . .   | 22 |
| 3.3 | A volume conductor consisting of homogeneous isotropic lung region in addition to heart and body surfaces [36]. . . . .  | 25 |
| 4.1 | The graph of RDM* error evaluated for the radial dipole closest to the innermost surface for several number of nodes. . . . .  | 36 |
| 4.2 | The graph of computation time needed to compute the potential distribution on the outermost surface for several number of nodes.   | 36 |

|     |   |    |
|-----|---|----|
| 4.3 | The inhomogeneous torso model used in the computations generated in <i>map3d</i> [27]. . . . .  | 38 |
| 4.4 | Potential distribution on a randomly selected point on the body surface for four different realistic models at several time instants.   | 39 |
| 4.5 | Potential distribution on a randomly selected point on the body surface for four different realistic models at several time instants.   | 40 |
| 4.6 | Potential distribution on a randomly selected point on the body surface for four different realistic models when the conductivity of the muscles have been decreased from 0.675 to 0.600. . . . . | 41 |
| 4.7 | Potential distribution on a randomly selected point on the body surface for four different realistic models when the conductivity of the lungshave been increased from 0.1 to 0.3. . . . .        | 42 |
| 5.1 | Solid angle subtended by a plane triangle at a point. . . . .   | 67 |
| 5.2 | Illustration of the integral element $dS/r$ . . . . .   | 69 |
| 5.3 | Adaptive numerical algorithm for evaluating surface integration [23]. . . . .   | 70 |

# CHAPTER 1

## INTRODUCTION

### 1.1 Motivation

The heart is the most considerable tissue of the body since it acts as a battery for us to live; therefore it has to be well behaved and kept. There is no problem when the heart is regularly working, however, in some cases when this regularity is corrupted by arrhythmias that sometimes cause fatal heart diseases (coronary heart disease, heart attack, congestive heart failure, endocarditis and myocarditis, cardiac arrhythmia etc. [60]). Death rate extrapolations in the USA for Cardiovascular diseases show that 945,836 people die every year, 78,819 per month, 18,189 per week, 2,591 per day, 107 per hour and 1 per minute [61], and 1.5 million people die from cardiovascular diseases every year in the EU [2]. It is projected that by 2025, approximately 60 % of the causes of death worldwide will be due to cardiovascular and circulatory diseases [60, 61].

Good news is that the heart diseases today are much more treatable than it used to be by the developing technology, progressive diagnosis and treatment, and impressive new gains are on the near horizon. Roger Kamm, a mechanical engineering professor who was himself involved in heart-disease studies in Massachusetts Institute of Technology (MIT), noted that there had been an explosion in the field of biomedical engineering over the past five years and the evolving state of heart-disease research had led to a wide range of efforts in the

field at MIT [3]. Like Kamm, many other scientists have seen the heart research so much worthwhile to deal for years. They have spent excessive effort and time to find methods of preventing people from heart diseases in any field such as bioinformatics, bioelectromagnetism, biomedical engineering, etc.

## **1.2 Purpose**

Being a part of the area of heart research, a thesis work has been accomplished by me. This work includes the concepts of electrocardiography, forward problem and boundary element method (BEM) using a realistic torso model in order to deal with effects of the torso inhomogeneities to the computations.

## **1.3 Scope**

This thesis report starts with background information including the mechanical and electrical activities in the heart, forward and inverse problems. It continues with the forward problem formulations for a homogeneous heart-torso model, and then, as an extension, with the forward problem calculations for an inhomogeneous heart-torso model. The main objective of this report, on one hand, is to present the effect of torso inhomogeneities to the potential distribution on the body surface when compared with the inhomogeneous case. On the other hand, the author shows how modern methods of applied mathematics can be successfully employed in an important area of medicine and health care.

# CHAPTER 2

## BACKGROUND

### 2.1 The Heart

#### 2.1.1 Anatomy of the Heart

The heart is a hollow, cone-shaped muscle located between the lungs and behind the sternum. Two-thirds of the heart is located to the left of the midline of the body and one-third is to the right (Figure 2.1).

The heart has 3 layers: The smooth inside lining of the heart is called the *endocardium*. The middle layer of heart muscle is called the *myocardium* which is surrounded by a fluid filled sac called as *pericardium* [8].

Inside of the heart is divided into four chambers, the two upper atria: Right Atrium (RA), Left Atrium (LA) and the two lower ventricles: Right Ventricle (RV), Left Ventricle (LV) (Figure 2.2).

#### 2.1.2 Mechanical Activity of the Heart

The right atrium receives de-oxygenated blood from the body through the superior vena cava (head and upper body) and inferior vena cava (legs and lower torso). The tricuspid valve, which separates the right atrium from the right ventricle, opens to allow the de-oxygenated blood collected in the right atrium

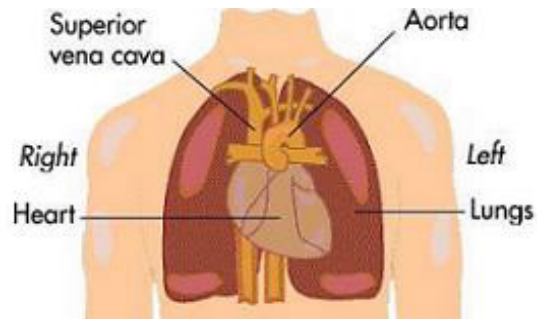


Figure 2.1: Location of the heart [8].

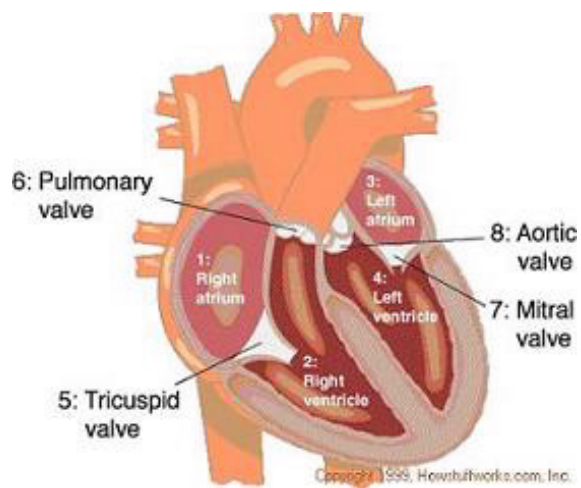


Figure 2.2: Anatomy of the heart [8].

to flow into the right ventricle. The right ventricle receives de-oxygenated blood as the right atrium contracts. The pulmonary valve leading into the pulmonary artery is closed, allowing the ventricle to fill with blood. Once the ventricles are full, they contract. As the right ventricle contracts, the tricuspid valve closes and the pulmonary valve opens. The closure of the tricuspid valve prevents blood from backing into the right atrium and the opening of the pulmonary valve allows the blood to flow into the pulmonary artery toward the lungs. The left atrium receives oxygenated blood from the lungs through the pulmonary vein. As the contraction triggered by the sinoatrial node progresses through the atria, the blood passes through the mitral valve into the left ventricle. The left ventricle receives oxygenated blood as the left atrium contracts. The blood passes through the mitral valve into the right ventricle. The aortic valve leading into the aorta is closed, allowing the ventricle to fill with blood. Once the ventricles are full, they contract. As the left ventricle contracts, the mitral valve closes and the aortic valve opens. The closure of the mitral valve prevents blood from backing into the left atrium and the opening of the aortic valve allows the blood to flow into the aorta and flow throughout the body [12].

### **2.1.3 Electrophysiology of the Heart**

The mechanical activity described above is accompanied by electrical activity in the heart. This activity begins with the Sinoatrial Node (SA Node) (Figure 2.3), which is a group of cells positioned on the wall of the right atrium, near the entrance of the superior vena cava. These cells have the ability to generate electrical activity on their own [8, 59] which yields a change in the electrical potential difference across the cell membrane. This dramatic change in the electrical potential is known as an *action potential* (AP) [37]. SA Node also known as the *pacemaker*. The heart also contains specialized fibers that conduct the electrical impulse initiated in the SA node to the rest of the heart. The electrical activity reaches the Atrioventricular Node (AV node), which is the sole muscular connection between the atria and ventricles [38]. The electri-

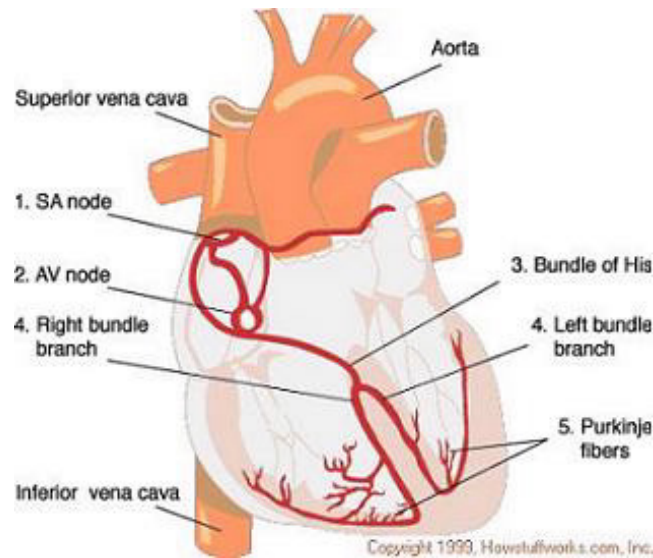


Figure 2.3: Electrical activity of the heart [8].

cal impulse now goes to the Bundle of His and, then, it divides into the Right and Left Bundle Branches where it rapidly spreads using Purkinje Fibers to the muscles of the Right and Left Ventricle, causing them to contract at the same time [8].

### Action, Epicardial and Electrocardiogram Potentials

The source of the electric currents and potential distributions inside the heart is the difference in the concentrations of positively and negatively charged ions – especially, ionic potassium - across the cell membranes. Initially, the resting inside-to-outside potential, the *transmembrane potential* (TMP) difference, is negative. A change of the ionic concentration could lead to a change in the direction of the TMP. If more ions flow out, the consequence is a more permeable membrane and a sudden breakdown of the resting potential, called *depolarization*, and an *action potential* (AP) (Figure 2.4).

Once a cell is depolarized, it can trigger neighboring cells and cause them to depolarize as well, producing a moving wavefront of varying electric potential, which is called as *activation wavefront*. As a result of the ion movements during

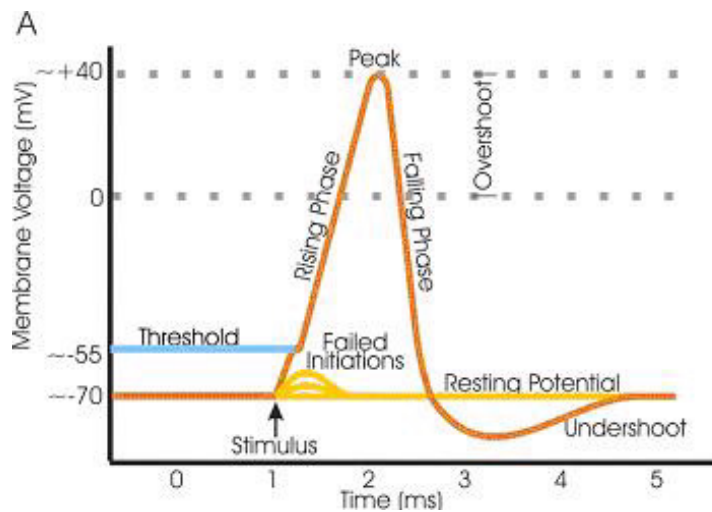


Figure 2.4: A schematic of an electrophysiological recording of an action potential showing the various phases which occur as the wave passes a point on a cell membrane [56].

depolarization, the calcium concentration inside the cell increases, causing the cell to mechanically contract, hence contracting the heart so that the blood is squeezed upwards and outwards from the ventricles in an effective manner. After one depolarization, there is an interval called the *refractory period*, during which a second depolarization cannot occur until after some degree of repolarization is complete. This ensures a minimum time interval between two consecutive mechanical contractions.

The potentials observed on the surface of the heart as a result of the electrical activities are known as *epicardial potentials*. These potentials differ from the transmembrane potentials, but instead respond to extracellular potential differences between regions of the myocardium.

Since the heart is in contact with the other compartments of the body, or torso, such as lungs, blood vessels, muscles, etc., the electrical currents do not stop, instead, propagate to the outward to the torso and their effect can be measured as distributions of electrical potentials on the body surface which are known as *body surface potentials* or *electrocardiogram potentials*. These potentials are measured by a device called *electrocardiograph* by placing different

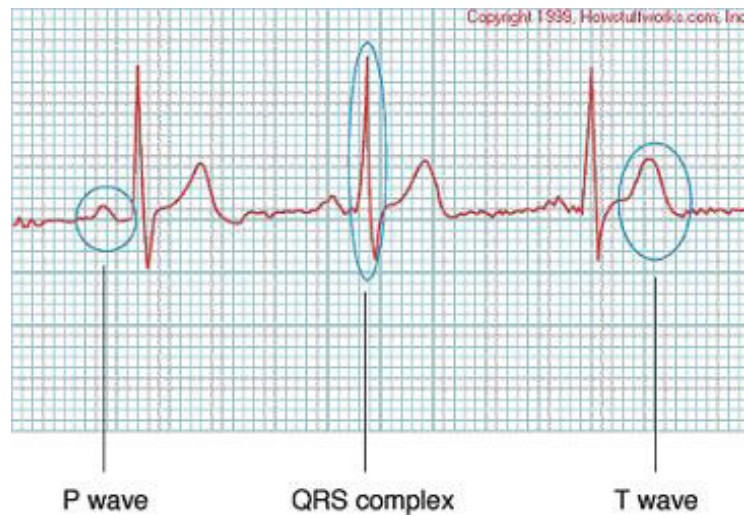


Figure 2.5: Electrocardiogram signal [57].

electrodes on the torso surface, which produces a graphical output showing the electrical voltage in the heart in the form of a continuous strip, called *electrocardiogram* [57]. Finally, electrocardiography (ECG, same abbreviation for electrocardiogram) is the technique used to record the electrical impulses which immediately precede the contractions of the heart muscle and relate the epicardial potentials with the resultant body surface potentials.

An electrocardiogram produces waves that are known as the *P*, *Q*, *R*, *S*, and *T* waves which gives each part of the ECG an alphabetical designation. As the heart beat begins with an impulse from the SA node, the impulse will first activate the upper chambers of the heart or atria and produce the *P* wave. Then the electrical current will flow down to the lower chambers of the heart or ventricles producing the *Q*, *R* and *S* waves. As the electrical current spreads back over the ventricles in the opposite direction it will produce the *T* waves (Figure 2.5).

Electrocardiogram is a common and relatively effective diagnostic tool and in addition, it has the advantages of being cheap and painless [10]. By observing the graph, the doctors

- can determine whether the heart is performing normally or suffering from

abnormalities (e.g., extra or skipped heartbeats - cardiac arrhythmia),

- may indicate acute or previous damage to heart muscle (heart attacks) or ischemia of heart muscle (angina),
- can detect potassium, calcium, magnesium and other electrolyte disturbances,
- can detect conduction abnormalities (heart blocks and in bundle branch blocks),
- can provide information on the physical condition of the heart (e.g., left ventricular hypertrophy, mitral stenosis) [57].

## 2.2 Forward and Inverse Problems of Electrocardiography

As noted in the previous section, the main objective of electrocardiography is to relate the potentials recorded at the body surface with the ones generated on the heart surface as a result of the electrical activity of the heart. Two different approaches - in other words, problems - are used in electrocardiography to establish this relation. The first approach is called the *forward problem* which entails the calculation of the body-surface potentials, starting usually from either pre-decided electrical representation of the heart activity (*equivalent current dipoles*) or from known potentials on the heart's surface (the epicardium) [20]. The other approach is the *inverse problem*, which involves the calculation of the potentials and prediction of the electrical activity of the heart starting from the potential distribution on the body surface, on the contrary to forward problem (Figure 2.6). The general objective of the forward and inverse problem of the electrocardiography is a better qualitative and quantitative understanding of the heart's electrical activity.

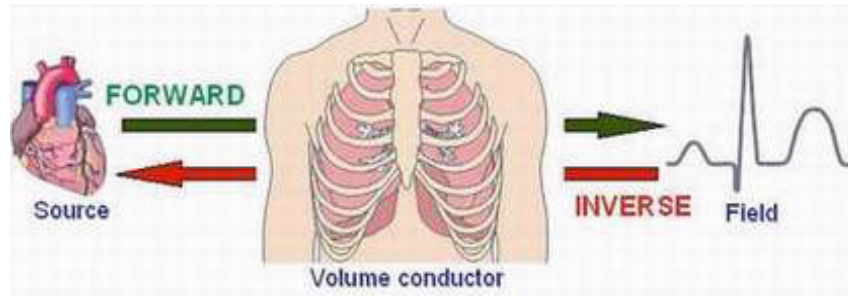


Figure 2.6: Schematic representation of the forward and inverse problem.

We have already stated that the current generated on the heart surface propagates through other conducting compartments (lungs, sternum, spines, skeletal muscle layer, and fat layer) of the torso so that the potential distribution measured on the body surface is directly affected by the geometrical and electrical properties of the torso compartments. Each of these compartments has different geometrical and electrical properties (conductivities). In the forward and inverse problem computations all these properties are taken into account in order to have a precise solution at the end.

Although forward and inverse problems differ by definition, these two problems are closely related with each other, since the complexity of the physiological torso model used must be tested through the forward solution and the inverse solution must be developed from the forward solution. For a specific solution to the forward or inverse solution of ECG, a three dimensional geometric description of a volume conductor (Figure 2.7) is required. The geometric description of the volume conductor can take several forms, depending on the specific method of mathematical solution [9].

When considering a realistic torso as in Figure 2.7, we have several regions which are physically different and have different electrical conductivities. This means that the volume conductor is *inhomogeneous*. Sometimes, in order to simplify the calculations, the conducting medium between the heart and body surface, inside of the torso, is assumed to be similar in geometry and have the same conductivity values. In that case, the torso is described as *homogeneous*.

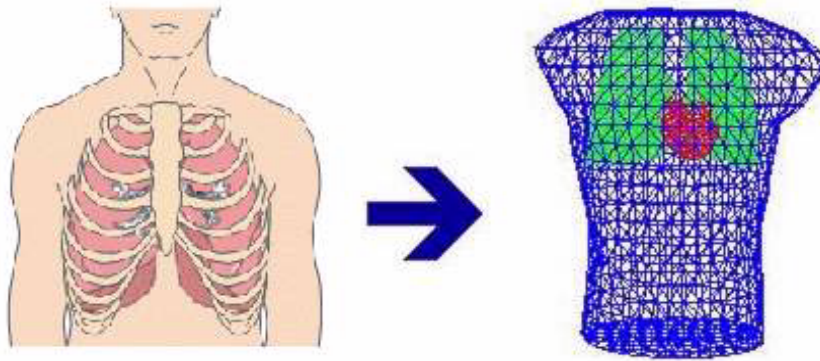


Figure 2.7: Geometric description of the volume conductor.

Moreover, if the conductivity value in a region changes with the direction then the region is defined to be *anisotropic*, otherwise, if the conductivity is constant over the region then the region is *isotropic*.

One of the key differences between the forward and inverse problems is that the forward solutions are generally unique; on the other hand, the inverse solutions are generally *not unique* [9]. Being not unique arises from the reason that the primary cardiac sources cannot be uniquely determined as long as the active cardiac region containing these sources is inaccessible for potential measurements. This is because the electric field that these sources generate outside any closed surface completely enclosing them may be duplicated by equivalent single-layer (monopole) or double-layer (dipole) current sources on the closed surface itself. Many equivalent sources and, hence, inverse solutions, are thus possible. However, once an equivalent source (and associated volume conductor) is selected, its parameters can usually be determined uniquely from the body-surface potentials [20].

One drawback of the inverse problems is that, computationally, inverse problems frequently involve complex numerical algorithms and large systems of equations. In addition, inverse problems are also typically *ill-posed*, that is, small changes in the input data can lead to deviations in the solutions. Often, the major challenge of an inverse problem lies in incorporating a priori information into the solution by regularizations and improvements [25]. The SCI Institute

has developed a number of efficient and realistic ways to solve a wide variety of inverse problems in functional imaging - including reconstruction of electrical sources within the heart or brain and extraction of molecular diffusion information from magnetic resonance images [31].

The content of this study does not include the inverse problem, but the forward problem of ECG. The above information has been given to make clear the two problems of ECG and relations, however, one can find a discussion on inverse problems in A.5.

### 2.2.1 Methods in the Forward Problem of ECG

The main motivation of forward problem of electrocardiography is to measure the body surface potentials from known epicardial potentials. This definition can be represented mathematically as follows:

$$P_B = Z_{BH} \cdot P_H. \quad (2.2.1)$$

Here,  $P_B$  is a vector of potentials on the body surface “to be measured”,  $P_H$  is a vector of “known” potentials on the heart surface,  $Z_{BH}$  is a transformation matrix determined from the geometrical coefficients and conductivities of the torso regions and  $\cdot$  denotes matrix multiplication.

Equation (2.2.1) is in the desired form for relating body surface potentials to those in the heart since this equation expresses the vector of potentials on the body surface as the product of a matrix of coefficients  $Z_{BH}$  times the vector of potentials on heart surface. In the remainder of this work, we will deal with the methods/approaches used in the forward problem of ECG in order to build the transformation matrix  $Z_{BH}$  from the geometry and conductivities.

In the forward problem of electrocardiography, one of the two general approaches is used, namely, *surface methods* and *volume methods*.

In surface methods, the different torso regions are assumed to be of isotropic

conductivity, that is the conductivity is constant over the region, and only the boundaries between the different regions are discretized and represented in the numerical torso model. These computations entail the solution of integral equations for the potential on the discretized surfaces of the torso model. Surface methods are also termed *boundary element methods* (BEM), since only the boundaries between torso regions are taken into consideration.

In volume methods, on the other hand, the entire three-dimensional torso model is represented numerically, usually by a combination of the tetrahedral and hexahedral (brick-shaped) elements. Volume methods may be subdivided into *finite-difference* (FDM), *finite-element* (FEM), and *finite-volume methods* (FVM).

Surface methods use simpler torso models with fewer elements. However, since the underlying integral equations couple the potential at every element to the potential at every other element. Volume methods use more complex torso models, with more elements and consequently more potentials to be determined. However, the potential at each point is expressed only in terms of the potentials at its nearest neighbors. Consequently, the coefficient matrix  $Z_{BH}$ , while large, is also sparse. Volume methods represent the only way to incorporate individual regions of varying conductivity.

The FEM, which is a volume based method, requires a complete volume mesh. The models that have used this method have tended to use a large number of low order (linear) finite elements. This, for the three-dimensional case, results in a large computational problem requiring vast computing resources. The FEM does, however, have the advantage of being able to easily cope with anisotropic, inhomogeneous regions.

The BEM, on the other hand, requires only a surface mesh. This reduces the number of elements required and, hence, the size and complexity of the model. The BEM also has the advantage in that it solves for the electrophysiologically important gradients (or currents) directly. The main limitation of this method for studying electrocardiography is that it can only be applied to isotropic re-

gions. However, there are works that applied BEM to anisotropic region as well [62].

## 2.3 Forward Problem and BEM in the Literature

### 2.3.1 Different Models

Electrocardiographic potentials and effects of inhomogeneities of the different torso regions have been studied theoretically, analytically and numerically in the literature. Preliminary studies consist of only the theoretical and primitive methods because of the lack of digital equipment and powerful computers. Analytical studies utilized the simple geometrical shapes in order to model the heart and the conducting volume where the heart is located. These studies were important in giving an idea; however, they were not sufficient in showing a real solution to the problem. Therefore, later studies used realistic heart and torso models and used numerical methods by discretizing the regions taken into account since analytical solutions cannot be applied to realistic geometries. Although, recent studies brought extra work and computing effort, by the technology that has improved fast in last decades, this problem has been nearly solved.

Most of the theoretical models of the heart-torso configuration were limited to a consideration of only a portion of the internal inhomogeneities [44]. The theoretical effect of the intracavitary blood mass on the body surface potentials was first studied by Brody and its effect on the dipolarity of an equivalent heart generator was investigated by Geselowitz and Ishiwatari. A theoretical investigation of the effect of lung and blood inhomogeneities was performed by Horacek, and by Arthur and Geselowitz. The surface muscle layer was modeled as a flat planar layer by McFee and Rush.

In addition to the studies depicted above, Rudy and Plonsey [44, 45] studied

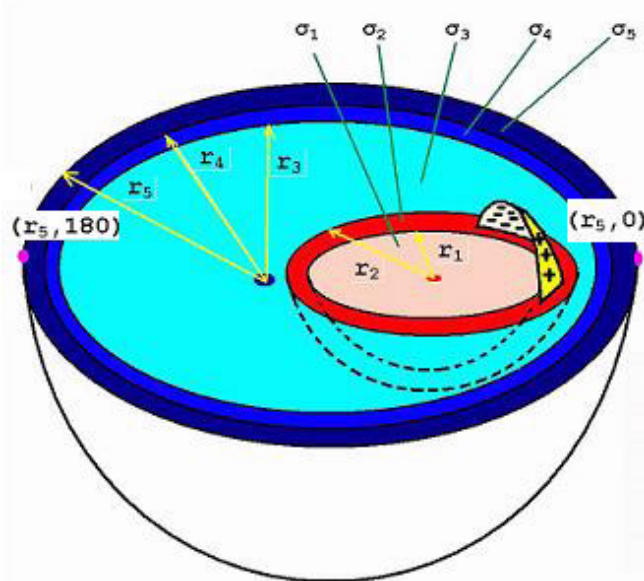


Figure 2.8: Eccentric spheres model [44].

the role of “all” internal geometry and inhomogeneities in the forward problem by modeling the heart and the conducting volume where the heart is immersed as “spheres” (Figure 2.8). An analytical solution, derived by considering only the boundaries of the torso compartments, was found that demonstrates the importance of interactions between the various torso compartments in determining the potential distribution at the body surface.

In this model, the heart is represented as a sphere consisting of a central blood volume bounded by a spherical heart-muscle cell and a pericardium; in turn, the heart is located eccentrically within a spherical torso, where the latter consists of a concentric lung region bounded by muscle and fat layers. Figure 2.8 shows the conductivity values ( $\sigma$ ) for all regions.

The key idea under this approach is that the spherical geometry is clearly a great idealization for obtaining an *analytical solution* to the problem. The main advantage of an analytical solution (compared to numerical methods) is the ability to include many layers in the model, and to manipulate the geometrical parameters easily. A numerical method [7, 36] requires a new discretization procedure whenever geometrical variations are introduced in the model.

Modeling as spherical or almost spherical geometry can be applicable to estimate cortical potentials from scalp potentials [23] since geometry holds for head model. However, in real world, heart and torso compartments do not have concentric spherical geometry. For this reason, analytical computations derived for these geometries do not hold for realistic heart and torso models. Anyway, they have been widely used to check the accuracy of the numerical solutions in the literature [33, 35, 46, 50].

### **2.3.2 Different Approaches**

Gulrajani and Mailloux [19] studied inhomogeneity by successively adding torso inhomogeneities to the torso model of Horacek which already incorporated lungs and intraventricular blood masses which have conductivities relative to the torso of 0.25 and 3.0, respectively. The first inhomogeneity added was the anisotropic homogeneous skeletal muscle layer. The trick about the skeletal muscle layer was that it had to be converted to an isotropic layer having a conductivity value of 0.625 relative to torso by a series of computations in order to be valid for boundary element calculations.

A better way to handle muscle layer and use the advantages of each of BEM and FEM is to use a coupled FEM/BEM approach [39, 45] which has been previously used by Stanley and Pilkington [51]. The model includes a number of torso inhomogeneities, namely the epicardium, lungs, skeletal muscle layer and subcutaneous fat layer. The BEM is used for isotropic and homogeneous regions of the torso (e.g., the lungs and torso cavity), and the FEM is used for anisotropic inhomogeneous regions (e.g., skeletal muscle layer).

# CHAPTER 3

## NUMERICAL SOLUTIONS

### 3.1 Numerical Solution for the Homogeneous Isotropic Torso Model

The determination of the body surface potential distribution from known epicardial potential distribution in a realistic-shaped torso is not applicable to be solved analytically since the region in account (heart and body) does not have a geometrically characteristic shape such as a sphere, ellipsoid, etc. For this reason, one must use a systematic way of solving this forward problem numerically by using one of the methods (FEM, BEM, FVM or FDM) described before.

In this section, a numerical solution technique, which includes the discretization of the regions in account and utilizes BEM, is presented. Based on this numerical method, a Matlab program has been developed. In the final section, the results of this computer program ran with a sample dataset will be discussed and analyzed.

#### 3.1.1 Motivation of the Method

As introduced before, the main goal of the forward problem of ECG is to relate the body surface potentials with the epicardial potentials. Based on this

definition, we can redefine the forward problem mathematically analogous to (2.2.1) as:

$$\Phi_B = Z_{BH} \cdot \Phi_H. \quad (3.1.1)$$

Here,  $\Phi_B$  is a vector of potentials on the body surface “to be measured”,  $\Phi_H$  is a vector of “known” potentials on the heart surface,  $Z_{BH}$  is a transformation matrix determined from the geometrical coefficients of the torso regions and  $\cdot$  denotes matrix multiplication.

Since,  $\Phi_H$  is already known and  $\Phi_B$  has to be determined, then one has to derive a transformation matrix  $Z_{BH}$  from the geometry of the torso regions in order to establish a relation between body surface and epicardial potentials.

Based on a schematical heart-torso model presented in the next section, Barr *et al.* [7] demonstrated the use of the boundary element method to find the potential at the body surface from known epicardial potentials.

The method of Barr is based on knowing the geometric location of each electrode, and on having enough electrodes to establish the geometric shape and potential distribution of closed epicardial and body surfaces. The method does not require that either the heart or body surfaces have any special shape, such as a sphere, or that any electrical quantities, such as voltage gradients, be known in addition to potentials.

The essence of this method is to find the coefficients that represent how potentials on the outer surface of a volume conductor can be computed as a linear combination of potentials on the inner surface. The method takes into account the consideration that the surfaces are defined by the known coordinates of a set of points on each surface. It is assumed that the volume conductor is homogeneous between the two surfaces, but that the conducting medium terminates at the outer boundary.

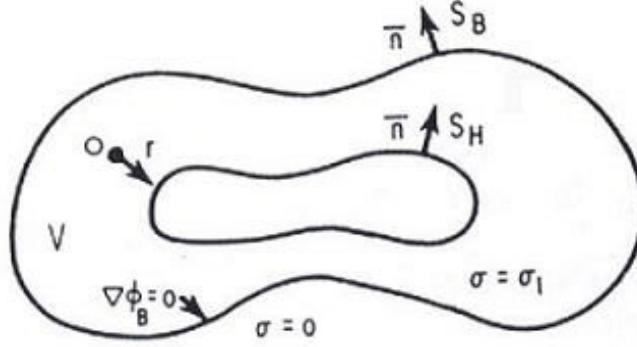


Figure 3.1: Homogeneous heart-torso model [7].

### 3.1.2 The Model

The homogeneous heart-torso model (Figure 3.1) takes two regions into consideration: The body surface (denoted as  $S_B$ ) and the heart surface (denoted as  $S_H$ ) with unit normal vectors  $n$ .

The torso region of interest is the volume  $V$  surrounded by the heart surface inside and the body surface outside. The inside volume is homogeneous and isotropic with a conductivity value  $\sigma = \sigma_l$ . The outer part of the body surface is air, so it has conductivity 0 (zero). Similarly, the inside region of the heart is assumed to have a zero conductivity because all the potentials are accumulated on the epicardium, the outer part of the heart. Here, the point  $O$  denotes an observation point inside the volume and  $r$  denotes the distance between the observation point and the surface element of integration inside the volume  $V$ . These definitions will be clearer in the following paragraphs.

Since, Figure 3.1 does not have a geometrical characteristic, such a sphere, ellipsoid, etc., an analytical solution is not possible for this model. Hence, we have to find a numerical solution for the transformation matrix  $Z_{BH}$  by using boundary element method as explained in the following subsection.

### 3.1.3 The Method of Solution

The method to be introduced in this section makes use of the BEM to solve the forward problem numerically. Because of this reason, as the BEM implies, the method only takes the “boundaries” of the heart and torso regions into consideration.

The method starts with analytical derivation of integral equations by applying Green’s second identity to the volume  $V$  in order to reduce the number of dimensions of the problem by one:

$$\int_S (A\nabla B - B\nabla A) \cdot n \cdot dS = \int_V (A\nabla^2 B - B\nabla^2 A) \cdot dV, \quad (3.1.2)$$

where, as identified in (3.1),  $V$  is a volume surrounded by the surface  $S$ , and  $n$  is an outward pointing vector of unit magnitude normal to the surface element  $dS$ . In addition,  $A$  and  $B$  are two scalar functions of position. Surface  $S$  is divided into two parts, one surrounded by the body surface,  $S_B$ , and the other surrounded by the heart surface,  $S_H$ .

This integral equation can be applied to our model by substituting the two scalar functions  $A$  and  $B$  in 3.1.2 with  $\Phi$ , the scalar electric potential inside the volume  $V$ , and  $1/r$ , the reciprocal of the distance between the observation point  $O$  and the surface of integration, respectively:

$$\int_S \left( \Phi \nabla \left( \frac{1}{r} \right) - \left( \frac{1}{r} \right) \nabla \Phi \right) \cdot n \cdot dS = \int_V \left( \Phi \nabla^2 \left( \frac{1}{r} \right) - \left( \frac{1}{r} \right) \nabla^2 \Phi \right) \cdot dV. \quad (3.1.3)$$

The details of the remaining analytical derivations, corresponding matrix definitions and determination of the transformation matrix  $Z_{BH}$  are presented in A.1.

The final equation that relates the epicardial to body surface potentials is:

$$\Phi_B = Z_{BH} \cdot \Phi_H,$$

where

$$Z_{BH} = (P_{BB} - G_{BH}G_{HH}^{-1}P_{HB})^{-1} (G_{BH}G_{HH}^{-1}P_{HH} - P_{BH}). \quad (3.1.4)$$

As mentioned before, the elements of matrix  $Z_{BH}$  are the “transfer coefficient matrices” [20] relating the potential at a particular epicardial surface point to that at a particular body-surface point and depend purely on the geometry of the epicardial and body surfaces. Here, the first subscript in each of the matrices  $P$  and  $G$  denotes location of the observation point and the second subscript denotes the surface where the integration is done.

### Determination of Matrices $P$ and $G$

The matrices  $P$  and  $G$  are coefficient matrices determined from the geometry. A combination of these matrices forms the final transformation matrix relating the epicardial potentials,  $\Phi_H$ , to the body surface potentials,  $\Phi_B$ .

The determination of matrices  $P$  and  $G$  is explained in [7] as the “iterative close and distant regions” (Figure 3.2) approach. This approach starts with the discretization in terms of triangles of the boundary surfaces and assumption that the potential is constant over each triangle element. Then, the apexes of the triangles are successively chosen as observation points. For every observation point, its effect on the integration triangle on the integration boundary surface is computed and the elements of the  $P$  and  $G$  matrices are evaluated as the weighted sum of these effects.

Figure 3.2 shows the discretization procedure of the boundary surfaces. In the first figure on the left, the surface is triangularized with the dot indicating the observer location. In this figure, in the middle, the surface is divided into “close” and “distant” regions. In other words, the total surface consisting of triangles having the observation point as an apex point is the *close region*,  $S_C$ , and each of the triangles that are not in the close region form the *distant region*,  $S_D$ .

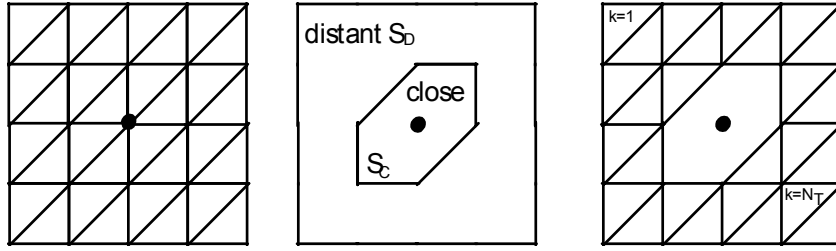


Figure 3.2: Diagrammatic surface used for considering how to construct coefficient matrices  $P$  and  $G$  [7].

Having defined the close and distance regions, each coefficient matrix  $P$  and  $G$  is determined in terms of the effects of each observation point on each of the triangle element in the distant and close region. The detailed method for determining each of the matrices  $P$  and  $G$  has been mentioned in [7].

One key point is that it is computationally advantageous to select as the unknowns not the potential at each triangle but rather the potential at each triangle vertex. Because, for most surfaces the number of triangle vertices is approximately half the number of triangles [42, 43], thus diminishing the size of the transformation matrix  $Z_{BH}$ .

If the method for determining the coefficients of the  $P$  and  $G$  matrices in [7] is observed well, the two important aspects can be seen from the integral equations: The evaluation of solid angle ( $\Omega$ ) subtended by a triangle at an observation point (see Appendix A.3) and integration over a plane triangle  $dS/r$  (see Appendix A.4).

## 3.2 Numerical Solution for the Inhomogeneous Torso Model

Having discussed the results of the forward problem using a homogeneous heart-torso model, we can, now, extend our study to a more realistic case. The model and the corresponding method introduced in the previous chapter

considered only two regions, heart and body surfaces. Since the homogeneous model assumes that the region between the heart and body surface is of the same property, the potential distribution on the body surface is not affected by the conductivity of the internal torso, which is not the case in reality. We know that the body consists of several compartments (lungs, bones, blood cavities, skeletal muscle layer, etc.) which have different geometrical and electrical properties. In realistic forward problem calculations, these regions have to be taken into account.

In this chapter, a numerical method based on the previous method with an extension of adding a homogeneous isotropic lung region to the previous homogeneous model is presented. A Matlab program has been developed for this inhomogeneous case and in the final section of this chapter; the results obtained from this computer program will be discussed and analyzed.

### 3.2.1 Motivation of the Method

Recalling from previous section, the main goal of the forward problem of ECG is to relate the body surface potentials with the epicardial potentials, which is mathematically defined as:

$$\Phi_B = Z_{BH} \cdot \Phi_H$$

where  $\Phi_B$  is a vector of potentials on the body surface “to be measured”,  $\Phi_H$  is a vector of “known” potentials on the heart surface, and  $Z_{BH}$  is a transformation matrix determined from the geometrical coefficients and the electrical conductivity values of the torso regions.

Since,  $\Phi_H$  is already known and  $\Phi_B$  has to be determined, one has to derive a transformation matrix  $Z_{BH}$  from the geometry of the torso regions in order to relate the body surface and epicardial potentials. Differently from the homogeneous case, the transformation matrix,  $Z_{BH}$ , is expected to depend on the geometrical property of the lungs, in addition to heart and body regions.

Another difference arises from the conductivities of the regions. Unlike the homogeneous heart-torso model, we have to take the conductivity values of the heart, body and isotropic homogeneous lung region into consideration, because the transformation matrix depends on the conductivities of the different regions.

Based on the definitions in the previous two paragraphs, the method of Barr *et al.* [7] has been extended to a more general one that can handle the inhomogeneities introduced in the model in the next section.

### 3.2.2 The Model

In order to relate the body-surface potentials to epicardial potentials in an inhomogeneous volume conductor, the model previously introduced by Barr *et al.* containing only the heart and body surfaces is now extended to have a homogeneous isotropic compartment, lung (Figure 3.3).

The surfaces labeled  $S_H$ ,  $S_L$  and  $S_B$  correspond to heart, lung, and body surfaces, respectively. The labels  $\sigma_H$ ,  $\sigma_L$ , and  $\sigma_B$  correspond to the conductivity values in the same manner. Additionally, the signs “+” and “-” show the conductivity values in the exterior and interior parts of the region in consideration.

Figure 3.3 can be further extended to have more inhomogeneities such as blood cavities, subcutaneous fat layer, epicardium, etc.

### 3.2.3 The Method of Solution

In general, the problem to be solved for the inhomogeneous case is analogous to the one of the homogeneous case. Motivation is to find a transformation matrix formed by geometry and conductivity properties of the different torso compartments which relates epicardial to body surface potentials.

The mathematical development of the transformation matrix for piecewise homogeneous torso is similar to that of the homogeneous formulation of Barr

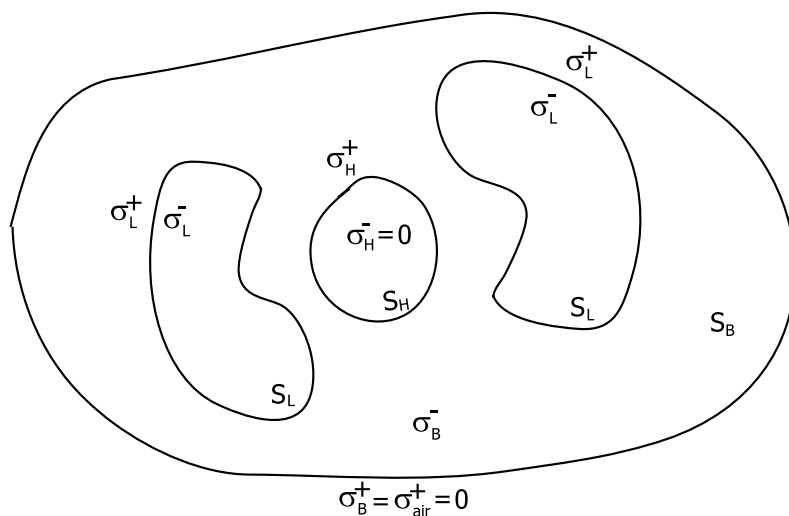


Figure 3.3: A volume conductor consisting of homogeneous isotropic lung region in addition to heart and body surfaces [36].

et al. [7], although conductivity interfaces are considered. Detailed derivations can be reached in Appendix A.2.

The relation between the body surface potentials with the epicardial potentials can be summarized by the following equation [36]:

$$\Phi_B = Z_{BH} \cdot \Phi_H.$$

Here,  $\Phi_B$  and  $\Phi_H$  are vectors of torso and epicardial potentials,  $Z_{BH}$  is a set of transfer coefficients which depend only on the geometry and conductivities of the epicardial and lung surfaces and  $\cdot$  denotes matrix multiplication.

The resulting set of transfer coefficients relating body surface potentials to

epicardial potentials is expressed by:

$$\begin{aligned}
Z_{BH} = & ((P_{BB} - G_{BH}G_{HH}^{-1}P_{HB}) & (3.2.5) \\
& + (P_{BL} - G_{BH}G_{HH}^{-1}P_{HL}) \\
& \cdot (P_{LL} - G_{LH}G_{HH}^{-1}P_{HL})^{-1} \\
& \cdot (G_{LH}G_{HH}^{-1}P_{HB} - P_{LB})^{-1} \\
& \cdot ((G_{BH}G_{HH}^{-1}P_{HH} - P_{BH}) \\
& + (G_{BH}G_{HH}^{-1}P_{HL}) \\
& \cdot (P_{LL} - G_{LH}G_{HH}^{-1}P_{HL})^{-1} \\
& \cdot (G_{LH}G_{HH}^{-1}P_{HH} - P_{LH})).
\end{aligned}$$

One can easily detect the analogy between the intermediate  $P$  and  $G$  matrices that form the transformation matrix in the inhomogeneous case and the one in the homogeneous case. The method of determination of  $P$  and  $G$  matrices is similar to that of the homogeneous case.

Stanley et al. [36] demonstrated the effect of including more homogeneities to the model introduced by Barr et al. [7]. The method of deriving the numerical solution when more inhomogeneities are included is similar to the one given in this section. The only difference is the increasing number of computations.

# CHAPTER 4

## RESULTS AND DISCUSSION

### 4.1 Method of Validation

In order to check the accuracy of the numerical solution derived in the previous chapters was compared with an analytical solution for concentric spheres introduced in [47]. The analytical solution utilizes a dipole with strength and orientation parameters and by using a series of weighted Legendre polynomials to find the electrical potential on the surface of the outermost sphere. Since, our numerical method relates the electrical potential on the outermost surface with the innermost surface, a potential distribution on the innermost surface is needed with the one on the outermost surface. Therefore, some changes were made on the analytical solution so that it provides a distribution of electrical potential on the given radius.

The procedure to check the accuracy of the numerical solution is as follows:

1. An electrical potential distribution has been computed on the innermost (the heart) and the outermost surface by using the analytical solution due to a dipole source model.
2. By using the numerical method, the transformation matrix  $Z_{BH}$  has been evaluated using only the geometry and conductivities.

3. The potential distribution on the heart surface,  $P_H$ , has been multiplied by  $Z_{BH}$  to find the potential distribution on the body surface,  $P_B$ .
4.  $P_B$  found in step 3 has been compared with the one evaluated in Step 1 by using the analytical solution.

The above procedure has been repeated for different dipole strengths and orientations, conductivity and radii values, and qualitative comparisons has been made including inhomogeneities to the model.

In order to validate the numerical solution, first, for given radii and conductivity values, the concentric spheres has been generated and, then, the potentials on the nodes on the innermost (matrix  $P_H$ ) and outermost surfaces (matrix  $P_B$ ) have been computed. Next, the same nodes have been triangulated to be used for the numerical solution. The triangulation has been done in such a way that the points on the line passing through the origin and intersecting the surfaces have been numbered the same. In other words, the point 81 on the outermost surface and same numbered point on the innermost and other surfaces are located on the same line that is passing through the origin. After the triangulation procedure, the transformation matrix,  $Z_{BH}$ , has been evaluated for the model. It has been expected to get a similar result for  $P_B$ , when multiplying the matrix  $P_H$  with the matrix  $Z_{BH}$ .

The accuracy of the numerical solution has been tested by using *Relative-Difference-Measure-Error* (*RDME*):

$$RDME = \sqrt{\frac{\frac{1}{n} \sum_{i=1}^n (P_i - T_i)^2}{\frac{1}{n} \sum_{i=1}^n T_i^2}}, \quad (4.1.1)$$

where  $P$  is a vector of numerically computed potentials for all the nodes on the body surface for a given dipole value, and  $T$  stands for the vector of analytically computed potentials for the same nodes according to the same dipole value. For a perfect fit,  $P = T$  and  $RDME = 0$ .  $RDME$  value shows how much

the “magnitudes” of the numerically computed potentials are different from the magnitudes of the analytically computed potentials.

Another metric used for the accuracy check is *Relative-Difference-Measure-Error-Star* ( $RDM^*$ ):

$$RDMSE = \sqrt{\sum \left( \frac{P_i}{\sum_{i=1}^n P_i^2} - \frac{T_i}{\sum_{i=1}^n T_i^2} \right)^2} \quad (4.1.2)$$

where  $P_{ij}$  and  $T_{ij}$  corresponds the ones in equation (4.1.1). Unlike RDME, RDMSE gives an idea about how much the “potential distribution patterns” received from the numerical differ from the ones from the analytical solution. The difference in the distribution patterns is much more important than the difference in the magnitudes of the potentials.

Next, in the realistic torso model, various inhomogeneities have been included in the model, and the effects of including or excluding the inhomogeneities have been discussed.

Finally, the intermediate matrices received during the numerical solution have been examined based on efficiency and singularity.

## 4.2 Validation of the Numerical Method

The validation procedure has been introduced in the previous section. In this section, based on the validation method, the accuracy of the numerical method will be checked for different models and dipole locations of different locations, strengths and orientations.

The dipole locations and orientations used in the computations have been generated by moving a dipole from the origin to the surface of the innermost layer step by step. The dipoles have both tangential and radial orientations. Additionally, the models used in the calculations are listed in Table 4.2.

Table 4.1: The dipole locations and orientations used in the computations: The values presented are in arbitrary units.

| Dipole No | Location $(x, y, z)$ | Orientation $(x, y, z)$ |
|-----------|----------------------|-------------------------|
| <b>1</b>  | 10, 0, 0             | 0, 0, 10                |
| <b>4</b>  | 40, 0, 0             | 0, 0, 10                |
| <b>7</b>  | 70, 0, 0             | 0, 0, 10                |
| <b>9</b>  | 90, 0, 0             | 0, 0, 10                |
| <b>19</b> | 30, 0, 0             | 10, 0, 0                |
| <b>21</b> | 50, 0, 0             | 10, 0, 0                |
| <b>23</b> | 70, 0, 0             | 10, 0, 0                |
| <b>24</b> | 80, 0, 0             | 10, 0, 0                |

Table 4.2: Spherical models used in the computations: The values are in arbitrary units.

|                       | Rad                | Cond             | NoN | NoT |
|-----------------------|--------------------|------------------|-----|-----|
| <b>M<sub>21</sub></b> | 100, 400           | 10, 1            | 132 | 260 |
| <b>M<sub>22</sub></b> | 100, 400           | 10, 1            | 380 | 756 |
| <b>M<sub>23</sub></b> | 100, 400           | 10, 1            | 501 | 998 |
| <b>M<sub>31</sub></b> | 100, 200, 400      | 10, 0.01, 1      | 132 | 260 |
| <b>M<sub>32</sub></b> | 100, 200, 400      | 10, 0.9, 1       | 132 | 260 |
| <b>M<sub>33</sub></b> | 100, 200, 400      | 10, 0.9, 1       | 501 | 998 |
| <b>M<sub>41</sub></b> | 100, 200, 300, 400 | 10, 0.9, 0.95, 1 | 132 | 260 |
| <b>M<sub>42</sub></b> | 100, 200, 300, 400 | 10, 0.9, 0.95, 1 | 380 | 756 |

In Table 4.1, the dipoles 1, 4, 7 and 9 are tangential; on the other hand, the dipoles 19, 21, 23 and 24 are radial dipoles. In Table 4.2,  $M$  denotes "the model", the first subscript denotes the "number of layers" (spheres) in the model and the second denotes the "index" of the model. Additionally,  $Rad$ ,  $Cond$ ,  $NoN$  and  $NoT$  refer to the "radii" of the layers from the innermost to the outermost layer, "conductivity" values of the layers in the same manner as radii, "number of nodes" and "number of triangles" on each layer, respectively.

Table 4.3 shows the result of the computations with respect to  $M_{21}$  (Table 4.2). Since, it is not feasible to give the results for all the nodes and dipole values, relatively more important cases have been chosen for discussion. In the following tables, the header *dipole* refers to the dipole value used in the calculation,  $A$  and

Table 4.3: Potential values of some points on the outermost surface calculated by analytical and numerical methods based on Model  $M_{21}$ .

| Dipole    | Analytic | Numeric | RDME    | RDMSE   |
|-----------|----------|---------|---------|---------|
| <b>1</b>  | -3.6425  | -3.6932 | 1.4340  | 0.0800  |
| <b>4</b>  | -3.6093  | -3.6380 | 0.8854  | 0.1947  |
| <b>7</b>  | -3.5387  | -3.4886 | 1.2147  | 0.3544  |
| <b>9</b>  | 0.0000   | 0.0015  | 1.1913  | 1.0237  |
| <b>21</b> | -0.2011  | -0.2323 | 1.7651  | 1.6049  |
| <b>24</b> | -0.3311  | -0.3654 | 1.8373  | 1.6283  |
| <b>26</b> | -0.4551  | -0.6659 | 7.8639  | 7.3163  |
| <b>27</b> | -0.5143  | -1.0807 | 19.9789 | 16.4658 |

$N$  refers to the potential value at an arbitrary node computed by analytical and numerical method, respectively. On the contrary, the *RDME* and *RDMSE* values are not specific to a potential value computed for a specific point, but for all the points on the outermost surface of the model.

Having observed the *RDME* and *RDMSE* values in Table 4.3, one can detect that the sudden increase in the *RDME* and *RDMSE* values for the dipoles 23 and 24 which are radial dipoles closest to the surface of the innermost layer.

The reason for the inaccuracy yielded from the location of the dipole inside the innermost surface is largely a quantization error. As the dipole location approaches the inner shell surface the potential field on the inner shell surface takes on an increasingly higher spatial frequencies. The node spacing on the inner shell is inadequate to represent these narrow fields. The error is greater for a radial dipole than for a tangential dipole because the potential field is more peaked [14]. Thus, the error should be reduced by increasing the number of nodes representing the innermost sphere.

Table 4.4 shows the results for the same model but with more nodes and triangles (model  $M_{22}$  in Table 4.2):

A more refined model,  $M_{23}$ , has given more accurate results (Table 4.5):

As observed, the error has been decreased by the increasing the number of nodes. The result is expectable, however, one should not forget that increas-

Table 4.4: RMSE and RDME values for the potential values calculated by analytical and numerical methods based on Model  $M_{22}$ .

| <b>Dipole</b> | <b>Analytic</b> | <b>Numeric</b> | <b>RDME</b> | <b>RDMSE</b> |
|---------------|-----------------|----------------|-------------|--------------|
| <b>1</b>      | -3.6425         | -3.6509        | 0.2520      | 0.0308       |
| <b>4</b>      | -3.6093         | -3.6144        | 0.1715      | 0.0792       |
| <b>7</b>      | -3.5387         | -3.5418        | 0.1478      | 0.1221       |
| <b>9</b>      | 0.0000          | 0.0002         | 0.3858      | 0.3611       |
| <b>19</b>     | -0.2011         | -0.2071        | 0.4753      | 0.4522       |
| <b>21</b>     | -0.3311         | -0.3343        | 0.4276      | 0.3859       |
| <b>23</b>     | -0.4551         | -0.4475        | 0.5709      | 0.4903       |
| <b>24</b>     | -0.5143         | -0.4517        | 3.1734      | 3.0119       |

Table 4.5: RMSE and RDME values for the potential values calculated by analytical and numerical methods based on Model  $M_{23}$ .

| <b>Dipole</b> | <b>Analytic</b> | <b>Numeric</b> | <b>RDME</b> | <b>RDMSE</b> |
|---------------|-----------------|----------------|-------------|--------------|
| <b>1</b>      | -3.6425         | -3.6480        | 0.1611      | 0.0231       |
| <b>4</b>      | -3.6093         | -3.6125        | 0.1086      | 0.0607       |
| <b>7</b>      | -3.5387         | -3.5403        | 0.0990      | 0.0935       |
| <b>9</b>      | 0.0000          | 0.0001         | 0.2874      | 0.2722       |
| <b>19</b>     | -0.2011         | -0.2055        | 0.3529      | 0.3386       |
| <b>21</b>     | -0.3311         | -0.3334        | 0.3155      | 0.2895       |
| <b>23</b>     | -0.4551         | -0.4501        | 0.4013      | 0.3448       |
| <b>24</b>     | -0.5143         | -0.4931        | 1.2531      | 1.1405       |

Table 4.6: RMSE and RDME values for the potential values calculated by analytical and numerical methods based on Model  $M_{31}$ .

| <b>Dipole</b> | <b>Analytic</b> | <b>Numeric</b> | <b>RDME</b> | <b>RDMSE</b> |
|---------------|-----------------|----------------|-------------|--------------|
| <b>1</b>      | -0.0866         | -0.0852        | 1.5642      | 0.1130       |
| <b>4</b>      | -0.0859         | -0.0841        | 2.1918      | 0.3538       |
| <b>7</b>      | -0.0845         | -0.0810        | 4.2118      | 0.5352       |
| <b>9</b>      | 0.0000          | 0.0016         | 4.2722      | 3.5192       |
| <b>19</b>     | -0.0041         | -0.0432        | 78.4508     | 66.4089      |
| <b>21</b>     | -0.0067         | -0.0517        | 89.8378     | 72.6534      |
| <b>23</b>     | -0.0092         | -0.2054        | 385.7946    | 122.5840     |
| <b>24</b>     | -0.0104         | -0.4616        | 879.3657    | 132.8023     |

ing the level of discretization means more computation time (10 seconds to 50 seconds in this example) [33].

Another discussion may arise from the relative conductivities of the compartments inside the volume conductor. Table 4.6 presents the RDME and RDMSE errors according to the model  $M_{31}$ . The middle layer inserted into the model  $M_{21}$  has a smaller conductivity value (0.01 units) than the one of the outermost layer (1 units). When the conductivity of the middle layer is increased to 0.9 units (Model  $M_{32}$ ), the decrease in the errors is observable and the result is corroborative to the idea that relatively small conductivity of one of the compartments compared with the conductivities of the other compartments yields considerable numerical errors [33]. In Table 4.7, the errors have been considerably reduced; however, further refinement can be done by increasing the number of nodes in the model (Table 4.8).

The errors and refinements for four-layer models have been shown in Tables 4.9 and 4.10.

Based on the above observations and results, it can be concluded that the accuracy of the numerical solution using BEM strictly depends on the dipole locations and orientations, and the difference between the conductivities of the layers. The former dependence arises when the dipole is a radial dipole (dipole 24) stationed very close to the surface of innermost layer. The tangential dipoles

Table 4.7: RMSE and RDME values for the potential values calculated by analytical and numerical methods based on Model  $M_{32}$ .

| Dipole    | Analytic | Numeric | RMDE    | RDMSE   |
|-----------|----------|---------|---------|---------|
| <b>1</b>  | -3.5016  | -3.5435 | 1.2399  | 0.0823  |
| <b>4</b>  | -3.4700  | -3.4910 | 0.6939  | 0.2040  |
| <b>7</b>  | -3.4027  | -3.3486 | 1.4127  | 0.3493  |
| <b>9</b>  | 0.0000   | 0.0015  | 1.1136  | 1.0376  |
| <b>19</b> | -0.1917  | -0.2228 | 1.7742  | 1.6926  |
| <b>21</b> | -0.3156  | -0.3495 | 1.8469  | 1.7307  |
| <b>23</b> | -0.4338  | -0.6430 | 8.2192  | 7.7558  |
| <b>24</b> | -0.4903  | -1.0504 | 20.7340 | 17.3577 |

Table 4.8: RMSE and RDME values for the potential values calculated by analytical and numerical methods based on Model  $M_{33}$ .

| Dipole    | Analytic | Numeric | RDME   | RDMSE  |
|-----------|----------|---------|--------|--------|
| <b>1</b>  | 3.5016   | 3.5050  | 0.1094 | 0.0239 |
| <b>4</b>  | 3.4700   | 3.4712  | 0.0736 | 0.0642 |
| <b>7</b>  | 3.4027   | 3.4026  | 0.1026 | 0.0996 |
| <b>9</b>  | 0.0000   | 0.0001  | 0.2787 | 0.2760 |
| <b>19</b> | -0.1917  | -0.1960 | 0.3556 | 0.3527 |
| <b>21</b> | -0.3156  | -0.3178 | 0.3085 | 0.3002 |
| <b>23</b> | -0.4338  | -0.4286 | 0.3780 | 0.3471 |
| <b>24</b> | -0.4903  | -0.4683 | 1.2715 | 1.1844 |

Table 4.9: RMSE and RDME values for the potential values calculated by analytical and numerical methods based on Model  $M_{41}$ .

| Dipole    | Analytic | Numeric | RDME    | RDMSE   |
|-----------|----------|---------|---------|---------|
| <b>1</b>  | 3.5303   | 3.5720  | 1.2213  | 0.0825  |
| <b>4</b>  | 3.4986   | 3.5192  | 0.6777  | 0.2051  |
| <b>7</b>  | 3.4310   | 3.3761  | 1.4263  | 0.3482  |
| <b>9</b>  | 0.0000   | 0.0015  | 1.1029  | 1.0328  |
| <b>19</b> | -0.1929  | -0.2238 | 1.7529  | 1.6758  |
| <b>21</b> | -0.3176  | -0.3512 | 1.8222  | 1.7110  |
| <b>23</b> | -0.4366  | -0.6456 | 8.1413  | 7.6840  |
| <b>24</b> | -0.4935  | -1.0539 | 20.5720 | 17.2147 |

Table 4.10: RMSE and RDME values for the potential values calculated by analytical and numerical methods based on Model  $M_{42}$ .

| Dipole    | Analytic | Numeric | RDME   | RDMSE  |
|-----------|----------|---------|--------|--------|
| <b>1</b>  | 3.5303   | 3.5336  | 0.1047 | 0.0240 |
| <b>4</b>  | 3.4986   | 3.4997  | 0.0719 | 0.0647 |
| <b>7</b>  | 3.4310   | 3.4308  | 0.1046 | 0.1004 |
| <b>9</b>  | 0.0000   | 0.0001  | 0.2768 | 0.2747 |
| <b>19</b> | -0.1929  | -0.1972 | 0.3520 | 0.3497 |
| <b>21</b> | -0.3176  | -0.3197 | 0.3051 | 0.2978 |
| <b>23</b> | -0.4366  | -0.4312 | 0.3750 | 0.3460 |
| <b>24</b> | -0.4935  | -0.4714 | 1.2617 | 1.1761 |

(dipole 9) do not affect the solution as the radial dipoles, because, the radial dipoles result a more peak potential. This dependence can be surpassed by increasing the number of nodes, relatively triangles in the model. Beside the increment of the number of nodes affect the accuracy in a positive manner, this solution may result in excessive computation time for the numerical method. Figure 4.1 represents how the refinement in the model affects the accuracy of the solution. In addition, Figure 4.2 shows the effect of refinement to the computation time of the numerical method. By observing the figures, one should make a choice on the degree of refinement to get reasonable results in reasonable duration. Moreover, the later dependence is especially the main problem of electroencephalography and magnetocardiography (EEG/MEG), where the conductivity of the skull is relatively small when compared to the brain. This problem may be solved by the *isolated problem approach* used in many studies [16, 17]. However, ECG studies does not face with this kind of problem.

### 4.3 Numerical Solution for Realistic Models

In this section, the numerical method derived in Chapter 3 has been utilized to compute the body surface potential distribution for a “realistic torso model”. The scheme presented in this section demonstrates the effects of torso inhomogeneities to the body surface potential distribution by not physically

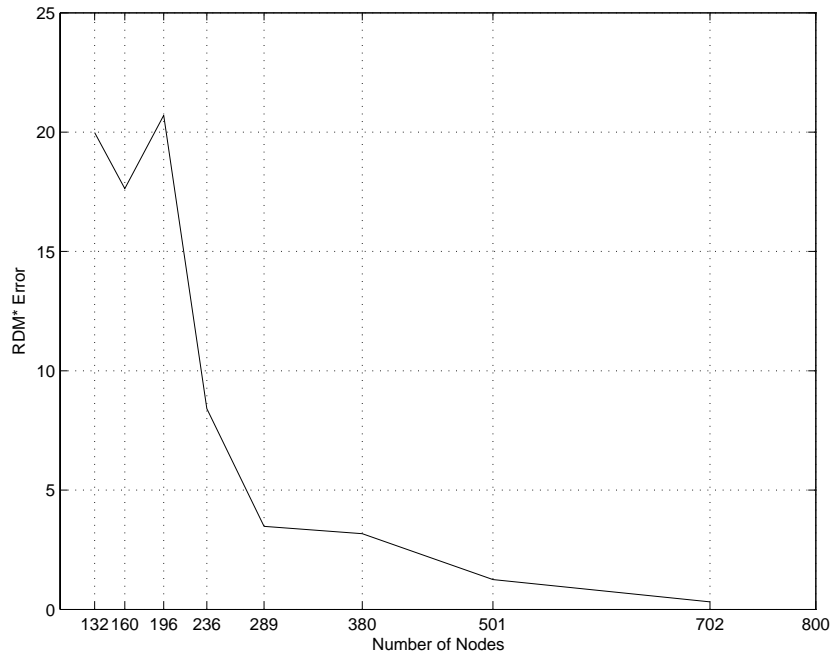


Figure 4.1: The graph of RDM\* error evaluated for the radial dipole closest to the innermost surface for several number of nodes.

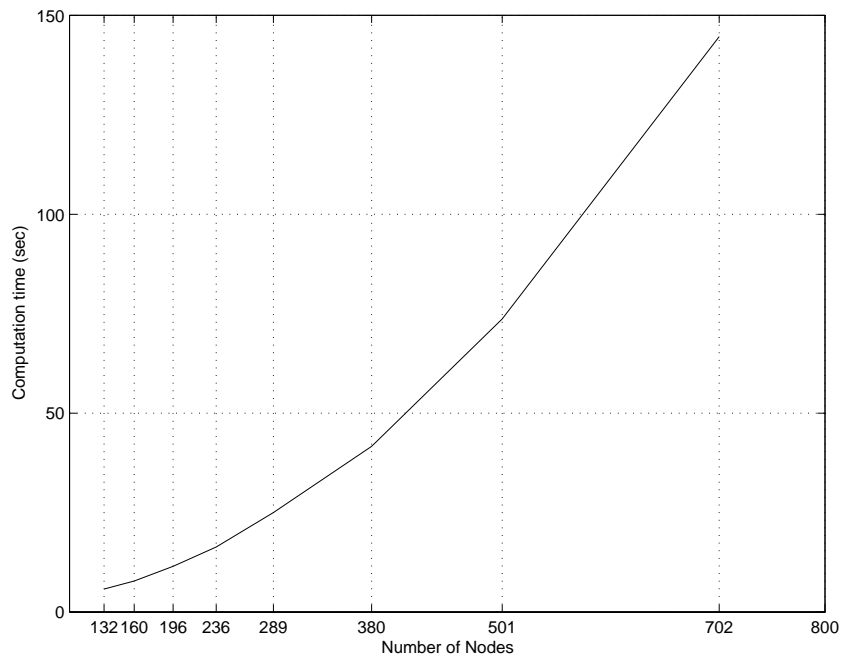


Figure 4.2: The graph of computation time needed to compute the potential distribution on the outermost surface for several number of nodes.

Table 4.11: Realistic models used in the computations: The values are in arbitrary units.

|              | $M_1$ | $M_2$      | $M_3$        | $M_4$             |
|--------------|-------|------------|--------------|-------------------|
| <b>Comp.</b> | H, B  | H, L, B    | H, M, B      | H, L, M, B        |
| <b>Cond</b>  | 10, 1 | 10, 0.1, 1 | 10, 0.675, 1 | 10, 0.1, 0.675, 1 |

including several inhomogeneities in the model. Instead, the models used in the experiments includes only lung region in the volume conductor, but with different conductivity values in each case. The models used in the computations are mentioned in Table 4.11.

In Table 4.11,  $M$  denotes “the model” and the subscripts refer to the “model number”. Additionally,  $Comp$  and  $Cond$  refer to the “compartments” included in the model and the “conductivity” values of the compartments in order, respectively. Finally, the labels  $H$ ,  $L$ ,  $M$  and  $B$  refers to the heart, lung, muscle and body surfaces, in the same manner. The heart surface has 289 nodes and 574 triangles, the lung surface has 652 nodes and 1296 triangles, and the muscle and body surfaces have 771 nodes and 1536 triangles.

An important note on the geometries of the compartments used in the following computations is that only the torso was realistically shaped. Because of the reason that the other compartments has been currently high-discretized (e.g., approximately 2000 nodes and 4000 triangles), the computation time would be incredibly long, therefore, it was not feasible to use those models. Instead, spherical geometries have been shifted, resized and rotated in or order to give the corresponding form to the compartments as in Figure 4.3.

In order to analyze the effect of different torso inhomogeneities to the body surface potential distribution on a realistic model, first, one needs an epicardial potential distribution. In this study, the necessary epicardial distribution has been generated by moving a dipole inside the heart. As a result, a potential distribution for 230 time instants has been computed.

The numerical results received from those four models in Table 4.11 have

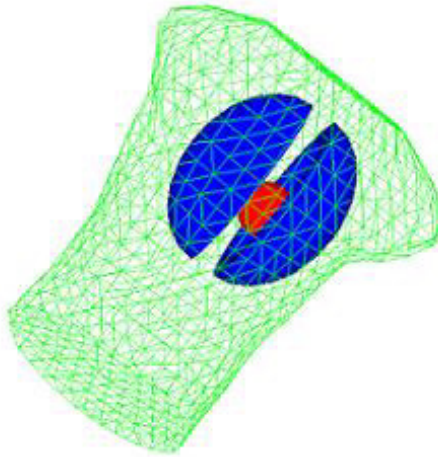


Figure 4.3: The inhomogeneous torso model used in the computations generated in *map3d* [27].

been figured by using graphs as in Figures 4.4 and 4.5. The figures precisely presents the effect of inhomogeneities to body surface potential distribution. Moreover, four different graphs in the same figure provides a comparative analysis of the effect of inhomogeneities.

At first sight, one can state that the potential values received from both models  $M_1$  and  $M_2$  are similar in magnitudes. Because, in both figures, the value for the potential values computed for the same time instants are almost the same or the difference is tiny. However, when the muscle region is in account,  $M_3$ , the change in the magnitudes of the potentials are apparent especially on the magnitudes of the peak potentials which are increased by the addition of the muscles. Finally, addition of both lungs and muscles,  $M_4$ , has changed the magnitudes of the potentials more than the single effect of muscles. Having in mind that the relative conductivity of the lungs and muscles has been chosen 0.25 and 0.675, respectively, it has been expected that the effect addition of the lungs should have been more visible than the effect addition of the muscles. Because of the reason that the lungs do not surround the heart, while the muscle region is parallel to the body surface and completely surrounds the heart and lungs, the change in the conductivity of the lungs do not considerably affect the body surface potential distribution. However, the change in the potential

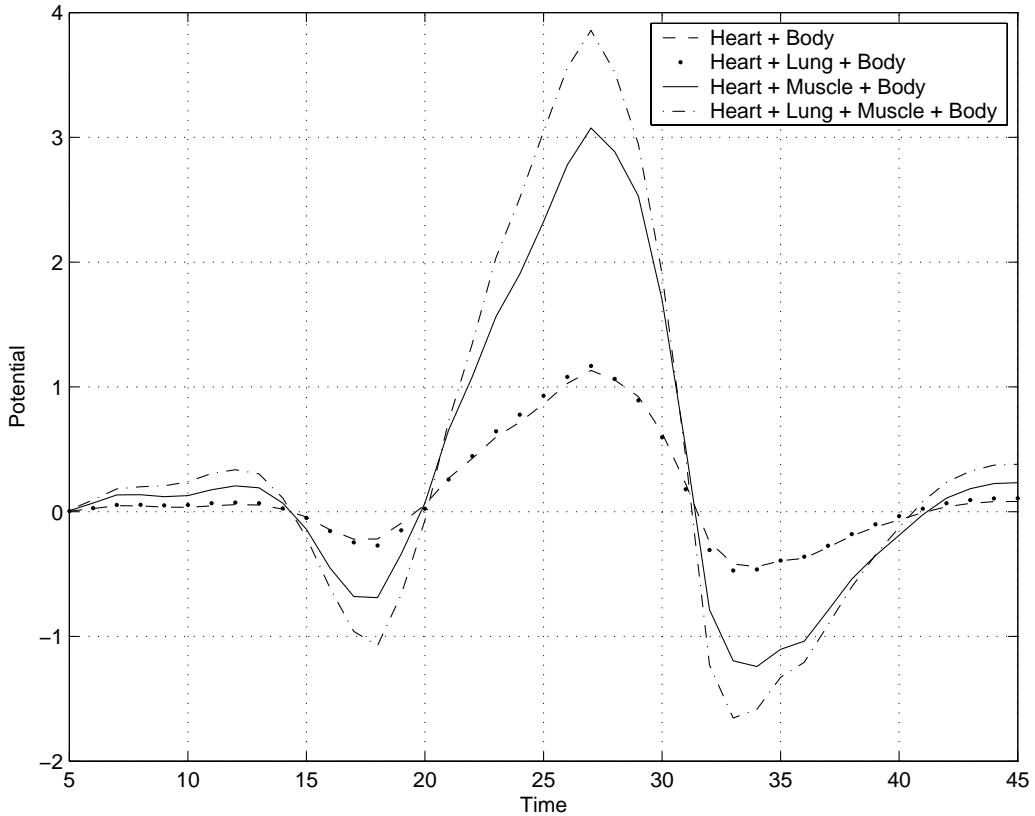


Figure 4.4: Potential distribution on a randomly selected point on the body surface for four different realistic models at several time instants.

magnitudes becomes considerable in case of a small change in the conductivity of the muscle region (Figure 4.6). Note that the peak potentials in Figure 4.6 have been increased when compared with Figures 4.4 and 4.5.

The same observation may be done by changing the effect of the change of the conductivity of the lungs to body surface potential distribution. In Model  $M_2$ , the conductivity of the lungs was chosen as 0.1. Figure 4.7 shows the resultant potentials for the same model, but the conductivity of the lungs has been chosen as 0.3 which is three times of the original. One should note that the peak potential have not been changed as much as in the case of decreasing the conductivity of the muscles.

Another discussion may be arisen on the change of potential distribution patterns. The body surface potential maps are not placed in this report, because

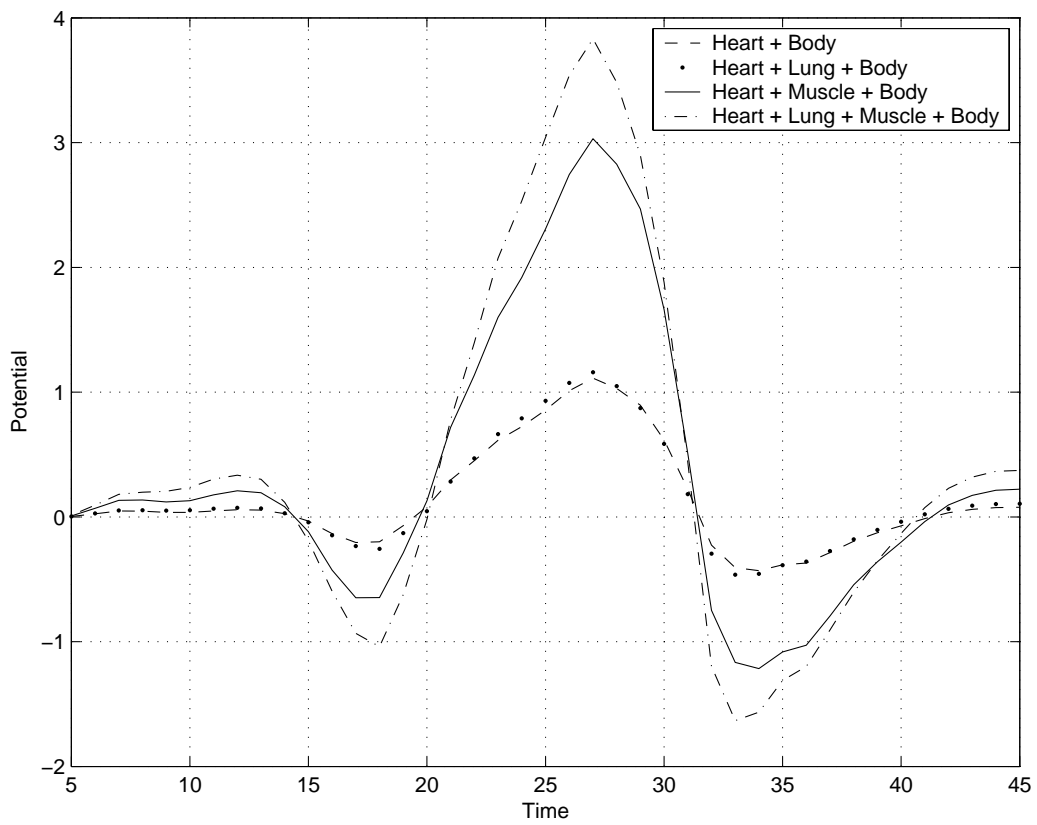


Figure 4.5: Potential distribution on a randomly selected point on the body surface for four different realistic models at several time instants.

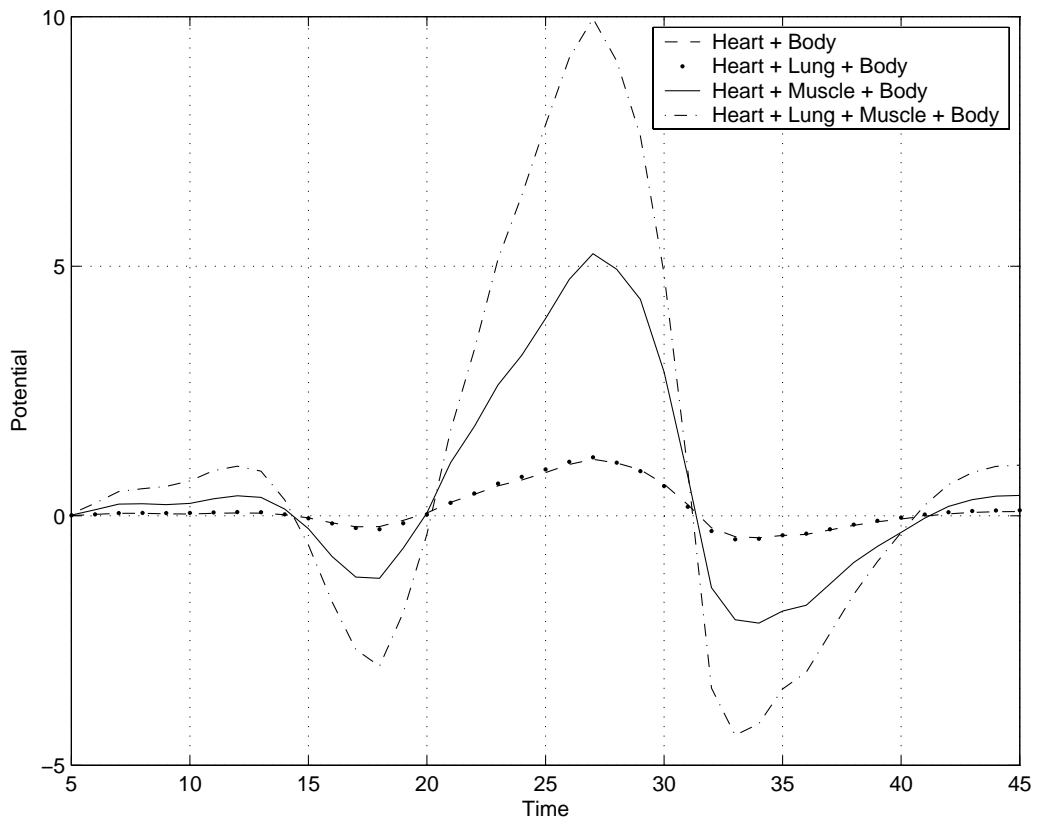


Figure 4.6: Potential distribution on a randomly selected point on the body surface for four different realistic models when the conductivity of the muscles have been decreased from 0.675 to 0.600.

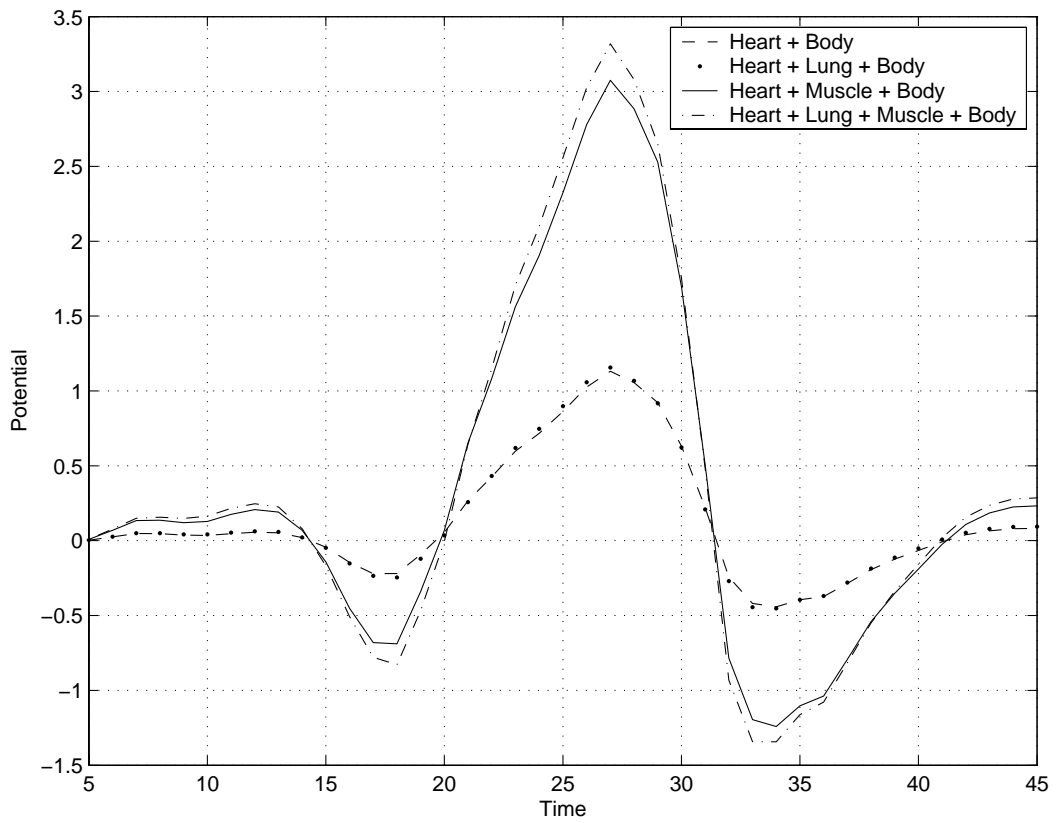


Figure 4.7: Potential distribution on a randomly selected point on the body surface for four different realistic models when the conductivity of the lungshave been increased from 0.1 to 0.3.

Table 4.12: The RDM\* values for realistic models.

|             | $M_1$ | $M_2 - M_1$ | $M_3 - M_1$ | $M_4 - M_1$ |
|-------------|-------|-------------|-------------|-------------|
| <b>RDM*</b> | -     | 1.535       | 6.294       | 6.257       |

the black-white print-out makes the low-resolution figures useless. Instead, the RDM\* error analysis used in the previous section has been utilized to observe the change in the potential distribution. Table 4.12 shows the numerical results from RDM\* analysis for all the points at all time instants. In other words, the RDM\* values have been calculated as the mean value of the RDM\* values for all the points for each of the 230 time instances. It can be concluded that the addition of muscles have yielded a considerable change in the potential distribution patterns, while the addition of lungs have a smaller effect than the one of muscles.

As a result of the discussions in this section, the main conclusion is that the effect of the muscles to the potential magnitudes and distribution patterns on the body surface is more visible than the one of lungs. The possible reason is that the muscle region completely surrounds the other compartments, while the lungs are simply a separated compartment like the others (i.e., heart, spine, sternum) and their effect is less than the one of muscle region. Another possible reason is that the space covered by the muscles is larger than the one of the lungs in the torso.

## 4.4 Examining the Intermediate Matrices

Remembering from the Equation (3.1.4) and (3.2.5),  $Z_{BH}$  is computed by multiplication, addition and, the most important, the inversion of some intermediate matrices. Each of these intermediate matrices is numerically computed by using the geometry and conductivity properties. The evaluation of these matrices includes the computation of solid angles subtended by triangles at observation points and the integrations over the area elements. These concepts

are discussed in Appendices A.3 and A.4.

In this section, the structure and evaluation of these matrices will be discussed.

The numerical solution was previously coded by using Matlab, which was a big fault. Because of the reason that, each  $(i, j)$  element of these matrices is computed by making a series of numerically discretized integral operations, the whole matrix is built up in  $i \times j$  iterations. Since Matlab is weak on element-by-element computations, the first task was to transform the code into C++. By this modification in the program, the computation time considerably decreased from tens of minutes to a few seconds. To give an example, the computation time to evaluate the transformation matrix for 3 spheres with 132 nodes and 260 triangles decreased from half an hour to 10 seconds. On the other hand, the matrix manipulation operations have been carried in Matlab; because, Matlab is extremely fast when compared to any program or tool. It is a common fact that Matlab has implicit fast and efficient matrix manipulation and optimization routines which makes it indispensable even for the cases when the matrices are large. This is explicitly proved during the thesis study by comparing the speed of matrix multiplication operations between two methods: one is Strassen's matrix multiplication coded in C++ and the other is simple matrix multiplication in Matlab. The adjective "simple" is used literally meaning that multiplication is simple in Matlab. Although, the Strassen's matrix multiplication algorithm is  $O(n^{2.81})$ , which is more efficient than the classical matrix multiplication algorithm of  $O(n^3)$ , the performance of Matlab was very reasonable. In fact Matlab is capable of multiplying two  $500 \times 500$  matrices in a reasonable time, while the other exhausts. As a result, after numerically computing the intermediate matrices in element-by-element manner in C++, the final transformation matrix is evaluated in Matlab.

The other criterion is the *matrix inversion* which is so sensitive to numerical errors especially when the matrices are sparse and ill-conditioned. Although, BEM is that BEM does not result in sparse matrices when being used in the

forward problem, the inversion problem has to be taken into consideration. Therefore, instead of directly taking the inverse of a matrix, one should solve a linear system of equations in closed form as follows:

$$A \cdot X = B, \tag{4.4.3}$$

where  $X$  can be replaced as the inverse of matrix  $A$ ,  $A^{-1}$ , and  $B$  as the identity matrix,  $I$ , for this work.

Successive elimination of variables, termed as *Gaussian elimination*, can be used to solve (4.4.3). However, this operation is  $O\left(\frac{n^4}{3} + \frac{n^3}{2}\right)$ . Instead, a decomposition scheme, which is the subject in consideration here, can be more useful and efficient. This technique is called *LU decomposition* because of the reason that it results in two triangular matrices such that:

$$A = L \cdot U, \tag{4.4.4}$$

where  $L$  is a lower triangular matrix and  $U$  is an upper triangular matrix.

This decomposition is useful, because the solution of triangular matrices is easily accomplished by successive substitution in the corresponding linear equations (starting with the corner of the triangle corresponding to a single non-zero term on the left side of the equation) as follows:

$$\begin{aligned} L \cdot U \cdot X &= B, & (4.4.5) \\ L \cdot Y &= B, \\ U \cdot B &= Y. \end{aligned}$$

First, the second sub-equation in (4.4.5)  $U \cdot X = Y$  is solved for  $Y$  by back substitution and then the third sub-equation is solved for  $X$  by the same approach [55]. The decomposition and back substitution procedures take  $O\left(\frac{4n^3}{3}\right)$  time, which is more efficient than Gaussian elimination.

Another advantage of the *LU* decomposition is that the resulting triangu-

lar matrices  $L$  and  $U$  can be overwritten on the matrix  $A$  if the matrices are computed such that the diagonal entries of the matrix  $L$  are 1. This situation makes the  $LU$  decomposition a “space-efficient” method because the diagonal entries of  $L$  is not need to be kept (4.4.6).

$$\begin{bmatrix} A_{11} & A_{12} & A_{13} & A_{14} \\ A_{21} & A_{22} & A_{23} & A_{24} \\ A_{31} & A_{32} & A_{33} & A_{34} \\ A_{41} & A_{42} & A_{43} & A_{44} \end{bmatrix} = \begin{bmatrix} U_{11} & U_{12} & U_{13} & U_{14} \\ L_{21} & U_{22} & U_{23} & U_{24} \\ L_{31} & L_{32} & U_{33} & U_{34} \\ L_{41} & L_{42} & L_{43} & U_{44} \end{bmatrix}. \quad (4.4.6)$$

The algorithm to find each  $L_{ij}$  and  $U_{ij}$  elements for a matrix  $A$  which has  $i$  rows and  $j$  columns has been given in equation (4.4.7) [18] as follows:

$$\begin{aligned} L_{ij} &= U_{jj}^{-1} \left( A_{ij} - \sum_{k=1}^{j-1} L_{ik} U_{kj} \right) & j \leq i - 1 \\ U_{ij} &= A_{ij} - \sum_{k=1}^{i-1} L_{ik} U_{kj} & j > 1 \end{aligned}. \quad (4.4.7)$$

It can be observed from that the algorithm may run into numerical inaccuracies if any  $U_{jj}$  becomes very small in the first line of (4.4.7). Thus the absolute values of  $U_{ii}$  are maximized if the rows of  $A$  are rearranged so that the absolutely largest elements of  $A$  in each column lie on the diagonal. The equations will become unchanged when the rows are rearranged, only the order will change. This approach is called *pivoting*.

In this study, Matlab’s  $lu()$  function has been utilized to find the inverses of the matrices such that:

$$[L, U, P] = lu(A), \quad (4.4.8)$$

where  $P \cdot A = L \cdot U$ . In (4.4.8),  $P$  is a permutation matrix to handle pivoting. Then, the inversion scheme takes the following form:

$$L \cdot U \cdot A^{-1} = P,$$

where

$$\begin{aligned}P &= L \cdot y, \\U \cdot A^{-1} &= y.\end{aligned}$$

The first of the above equations can be solved for  $y$  and, later, the second can be solved for  $A^{-1}$ .

# CHAPTER 5

## SUMMARY AND CONCLUSION

The heart is the most important tissue in the body, because it acts as a battery. It pumps the clean oxygenated blood, which is needed by tissues for respiration, to the body by the help of the surrounding epicardial muscles. This operation is repeated periodically, approximately 80 times per minute in a healthy person at rest. This mechanical activity in the heart is initiated and driven by specialized cells which are capable of generating electrical currents. The currents further move outward to the body surface, where they result a potential distribution measured by medical tools. The potential distribution generated on the body surface are called *electrocardiogram potentials* or *body surface potentials*.

In order to understand the behaviour of the heart, its wellness or defections, one needs an accurate relation between these potential distributions. The electrocardiography is the technique to deal with the potential distributions on the heart and on the body.

Electrocardiography utilizes two problems: the *forward problem* and the *inverse problem*. The main motivation of the former one is to estimate the potential distributions on the body surface from the corresponding potentials on the heart surface. The later one, inverse problem, deals with the determination

of the epicardial potentials from the measured body surface potentials.

Mathematically, the forward problem is represented as follows:

$$P_B = Z_{BH} \cdot P_H,$$

where  $P_B$  and  $P_H$  are the matrices including the information of the potential distribution on the body surface and on the heart surface, respectively. On the other hand,  $Z_{BH}$  is a transformation matrix determined from the geometry and conductivity properties.

The forward problem mainly presents two kind of methods, namely *surface* and *volume methods*. In surface methods, also called *boundary element methods* (*BEM*), only the boundaries of the torso regions are taken into consideration, whereas, the volume methods needs the whole volume to be discretized.

Based on the above summary, the content of this study includes the BEM formulation and its solution using realistic torso models. Since the analytical solution is not possible for a realistic models, first, the problem has been solved by using concentric spherical models. This method is widely referred in the literature to check the accuracy of the numerical methods. The approach presented to check the accuracy of the numerical method derived in Chapter 3 has started with the positioning of the tangential and radial dipoles into the innermost sphere and receiving a potential distribution on both the heart and body surface. Next, the transformation matrix has been evaluated with the numerical method. Finally, the potential distribution on the heart surface is transformed to the one on the body surface and the results of both numerical and analytical method have been compared.

The comparisons have pointed out that the accuracy of the BEM strictly depends on the dipole positions and orientations, and the differences between the conductivities of the layers in the model. When the dipole is radial and close to the inner boundary and the conductivity of one of the layers is relatively small when compared to others, the numerical method yields considerable

errors. The first problem can be solved by increasing the number of nodes (and also triangles) on the innermost boundary, and the later, by isolated problem approach, which has not been mentioned in this study.

After the validation of the numerical method, in order to analyze the effects of the inhomogeneities in a realistic torso model, a few observations have been accomplished with the relatively higher discretized boundaries compared to ones in the homogeneous case in order to decrease the possible numerical error.

The effects of torso inhomogeneities has been studied in many ways [19, 36, 44, 45, 62]. The general idea is that the presence of lungs has a minimal effect on the body surface potential distribution. As in the general sense, this work presents that the lungs have minimal effect in the relation between epicardial and body surface potentials, while the muscles have more considerable effects on body surface potential distribution.

This work consists of considerable mathematical information, besides its biomedical engineering side. The discussions on matrix manipulation operations, such as multiplication and inversion, and the establishments on efficiency constraints on building the matrices, the observations on the computation of solid angles and integration over surfaces and discretization procedures etc. light the way for the people who work or willing to work on these concepts in their disciplines.

# REFERENCES

- [1] Akçelik, V., Biros, G. and Ghatta, O., Parallel multiscale Gauss-Newton-Krylov methods for inverse wave propagation, Proceedings of the 2002 ACM/IEEE Conference on Supercomputing, pp. 1-15, 2002.
- [2] Annual Report, 2000, The European Heart Network,  
<http://www.ehnheart.org/files/Ehn2000-134334A.pdf>.
- [3] Anthony, R., The power of hope - The promise of heart research, Spectrum, Massachusetts Institute of Technology,  
<http://web.mit.edu/giving/spectrum/spring98/hope.html>.
- [4] Aster, R., Borchers, B. and Thurber, C., Parameter estimation and inverse problems, October 2, 2003.
- [5] Babaeizadeh, S. and Brooks, D.H., Boundary element methods for electrocardiography, Communications and Digital Signal Processing Center for Research and Graduate Studies, CDSP Poster, May 2003.
- [6] Babaeizadeh, S., Brooks, D.H. and Isaacson, D., A 3-D boundary element solution to the forward problem of electrical impedance tomography.
- [7] Barr, R.C., Ramsey, M. and Spach, M.S., Relating epicardial to body surface potential distributions by means of transfer coefficients based on geometry measurements, IEEE Trans. Biomed., Vol. BME-24, No. 1, January 1977.
- [8] Bianco, C., How Your Heart Works,  
<http://www.howstuffworks.com/heart.htm>.

- [9] Bradley, C.P. and Pulan, A.J., The forward problem of electrocardiology, Proceedings of the 2nd NZ Postgraduate Conference for Engineering and Technology Students, pp. 34-39, 1995.
- [10] Brooks, D.H. and Macleod, R.S., Electrical imaging of the heart, IEEE Signal Processing, 14(1): 24-42, January 1997.
- [11] Burghignoli, P., Pajewski, L., Frezza, F., Galli, A. and Schettini, G., Improved quadrature formulas for boundary integral equations with conducting or dielectric edge singularities, IEEE Trans. of Antennas and Prop., Vol. 52, No. 2, February 2004
- [12] Cardiovascular Consultants, Heart Anatomy, <http://www.cardioconsult.com/Anatomy>.
- [13] De Munck, J.C., A linear discretization of the volume conductor boundary integral equation using analytically integrated elements, IEEE Trans Biomed Eng., Vol. 39(9), pp. 986-90, September 1992.
- [14] Ferguson, A.S. and Stroink, G., Factors affecting the accuracy of the boundary element method in the forward problem—I: Calculating surface potentials, IEEE Trans Biomed Eng., Vol. 44(11), pp. 1139-55, November 1997.
- [15] Ferguson, S., Zhang, X. and Stroink, G., A complete linear discretization for calculating the magnetic field using the boundary element method, IEEE Trans. Biomed. Eng., Vol. 41(5), pp. 455-60, May 1994.
- [16] Fuchs, M., Drenckhahn, R., Wischmann, H.A. and Wagner, M., An improved boundary element method for realistic volume-conductor modeling, IEEE Trans. on Biomed. Eng., Vol. 45, No. 8, August 1998.
- [17] Gençer, N.G. and Akalın-Acar, Z., Use of isolated problem approach for the multi-compartment BEM models of Electric source imaging, Phys Med Biol., Vol. 50(13), pp. 3007-22, July 2005.
- [18] Mike Guidry and Mike Strayer, Linear algebra notes: LU Decomposition, [http://csep10.phys.utk.edu/guidry/phys594/lectures/linear\\_algebra/lanotes/node3.html](http://csep10.phys.utk.edu/guidry/phys594/lectures/linear_algebra/lanotes/node3.html)

- [19] Gulrajani, R.M. and Mailloux, G.E. A simulation study of the effects of torso inhomogeneities, *Circulation Research*, Vol. 52, pp. 45-56, 1983.
- [20] Gulrajani, R.M., The forward and inverse problems of electrocardiography, *IEEE Eng Med Biol Mag.*, pp. 17:84-101,122, 1998.
- [21] Gulrajani, R.M., The forward problem of electrocardiography: From heart models to body surface potentials, *Proceedings – 19th International Conference – IEEE/EMBS October 30 – November 2, 1997.*
- [22] Hansen, P.C., *Regularization Tools A Matlab Package for Analysis and Solution of Discrete Ill-Posed Problems, Version 3.1 for Matlab 6.0*, 1998.
- [23] He, B., Wang, Y. and Wu, D., Estimating cortical potentials from scalp EEG's in a realistically shaped inhomogeneous head model by means of the boundary element method, *IEEE Trans. Biomed. Eng.*, Vol. 46, No. 10, October 1999.
- [24] Heller, L., Computation of the return current in encephalography: The auto solid angle", *Digital Image Synthesis and Inverse Optics, Proc. SPIE 1351*, pp. 376-90, 1990.
- [25] Huiskamp, G. and van Oosterom, A., The depolarization sequence of the human heart surface computed from measured body surface potentials, *IEEE Trans. Biomed. Eng.*, Vol. 35, No. 12, December 1988.
- [26] Hunter, P. and Pullan, A., *FEM/BEM Notes*, February 19, 2002.
- [27] Macleod, R.S. and Johnson, C.R., *Map3d: Interactive scientific visualization for bioengineering data, Datasets*, <http://software.sci.utah.edu>.
- [28] Macleod, R.S. and Johnson, C.R., *Map3d: Interactive scientific visualization for bioengineering data, IEEE Engineering in Medicine and Biology Society 15th Annual International Conference*, IEEE Press, pp. 30-31, 1993.

- [29] Macleod, R.S., Formulation of a forward problem of electrocardiography using the boundary element method, <http://www.cvrti.utah.edu/~macleod/talks/bem-form>.
- [30] Macleod, R.S., Gardner, M., Miller, R.M. and Horacek, B.M., Application of an electrocardiographic inverse solution to localize ischemia during coronary angioplasty, *J. Cardiovasc Electrophysiol.*, Vol. 6(1), pp. 2-18, January 1995.
- [31] Macleod, R.S., Research at the SCI Institute, <http://www.sci.utah.edu/research/research.html>.
- [32] McFee, R. and Rush, S., Qualitative effects of thoracic resistivity variations on the interpretation of electrocardiograms: the low resistance surface layer, *Am Heart J.*, Vol. 76(1), pp. 48-61, July 1968.
- [33] Mejis, J.W.H., Weier, O.W., Peters, M.J. and van Oosterom, A., On the numerical accuracy of the boundary element method, *IEEE Trans. Biomed. Eng.*, Vol. 36, No. 10, pp. 1038-49, October 1989.
- [34] Neilson, L.A. and Koles, Z.J., The finite volume head model for EEG source localization, *Int. J. Bioelectromagnetism*, Vol. 4, No. 2, pp. 149-50, 2002.
- [35] Oostendorp, T. and van Oosterom, A., The potential distribution generated by surface electrodes in inhomogeneous volume conductors of arbitrary shape, *IEEE Trans Biomed Eng.*, Vol. 38(5), pp. 409-17, May 1991.
- [36] P.C. Stanley, T.C. Pilkington and M.N. Morrow, The effects of thoracic inhomogeneities on the relationship between epicardial and torso potentials, *IEEE Trans Biomed Eng.*, Vol. 33(3), pp. 273-84, March 1986.
- [37] Patino, F.C., Level Sets Applied to Inverse Problem in Electrocardiography, Universitat Politcnica de Catalunya, October 10th, 2004.
- [38] Plonsey, R., *Bioelectric Phenomena*, New York: McGraw-Hill, 1967.

- [39] Pullan, A.J. and Bradley, C.P., A computational procedure for modeling electrical activity from heart to body surface, Proceedings – 19th International Conference – IEEE-EMBS, October 30 – November 2, 1997.
- [40] Radon, J., Zur mechanischen Kubatur, Monat. Mathematik, vol. 52, pp. 286–300, 1948.
- [41] Rao, L., He, R., Liu, Y.S. and Yan, W., Computations of electroencephalography and magnetoencephalography for real head model, IEEE Transactions on Magnetics, Vol. 36, No. 4, July 2000.
- [42] Rossignac, J., Edgebreaker - Connectivity compression for triangle meshes, GVU Technical Report GIT-GVU-98-35.
- [43] Rossignac, J., Safonova, A. and Szymczak, A., 3D compression made simple: Edgebreaker on a corner-table, Invited lecture at the Shape Modeling International Conference, Gemoa, Italy. May 7-11, 2001.
- [44] Rudy, Y. and Plonsey, R., The eccentric spheres model as the basis for a study of the role of geometry and inhomogeneities in electrocardiography, IEEE Trans. Biomed. Eng., vol. 26, pp. 392-99, 1979.
- [45] Rudy, Y. and Plonsey, R., The effects of variations in conductivity and geometrical parameters on the electrocardiogram, using an eccentric spheres model, Circ. Res., Vol. 44, No. 1, pp. 104-11, 1979.
- [46] Schlitt, H.A., Heller, L., Aaron, R., Best, E. and Ranken, D.M., Evaluation of boundary element methods for the EEG forward problem: effect of linear interpolation, IEEE Trans Biomed Eng., Vol. 42(1), pp. 52-8, January 1995.
- [47] Silva, F.H.L. da, Boom, H.B.K. and Spekreijse, I.H., The inverse problem in EEG and MEG with applications to visual evoked responses, Cornelis Johannes Stok, 1986.
- [48] Soleimani, M., Powell, C.E. and Polydorides, N., Improving the forward solver for the complete electrode model in EIT using algebraic multigrid, IEEE Trans. Med. Imaging, Vol. 24(5), pp. 577-83, May 2005.

- [49] Srebro, R., A modified boundary element method for the estimation of potential fields on the scalp, *IEEE Trans. Biomed. Eng.*, Vol. 43(6), pp. 650-3, June 1996.
- [50] Srinivasan, R., Methods to improve the spatial resolution of EEG, *Int. J. of Bioelectromagnetism*, Vol. 1, No. 1, 1999.
- [51] Stanley, P.C. and Pilkington, T.C., The combination method: a numerical technique for electrocardiographic calculations, *IEEE Trans. Biomed. Eng.*, Vol. 36(4), pp. 456-61, April 1989.
- [52] Tissari, S. and Rahola, J., A precorrected-FFT method to accelerate the solution of the forward problem in magnetoencephalography, *Phys. Med. Biol.*, Vol. 48, pp. 523-41, 2003.
- [53] Van Oosterom, A. and Strackee, J., The solid angle of a plane triangle, *IEEE Trans. Biomed. Eng.*, Vol. 30, pp. 125-26, 1983.
- [54] Van Oosterom, A., Solidifying the solid angle, *J. Electrocardiol.*, Vol. 35, pp. 181-92, 2002.
- [55] Weisstein, E.W., LU decomposition, *MathWorld—A Wolfram Web Resource*,  
<http://mathworld.wolfram.com/LUDecomposition.html>.
- [56] Wikipedia contributors, Action potential, *Wikipedia - The Free Encyclopedia*, 2006,  
[http://en.wikipedia.org/wiki/Action\\_potential](http://en.wikipedia.org/wiki/Action_potential).
- [57] Wikipedia contributors, Electrocardiogram, *Wikipedia - The Free Encyclopedia*, 2005,  
<http://en.wikipedia.org/wiki/Electrocardiogram>.
- [58] Wikipedia contributors, Heart, *Wikipedia - The Free Encyclopedia*, 2006,  
<http://en.wikipedia.org/wiki/Heart>.

- [59] Wikipedia contributors, Sinoatrial node, Wikipedia - The Free Encyclopedia, 2006,  
[http://en.wikipedia.org/wiki/Sinoatrial\\_node](http://en.wikipedia.org/wiki/Sinoatrial_node).
- [60] World Heart Report, 2003, American Heart Association,  
[http://www.who.int/entity/whr/2003/en/whr03\\_en.pdf](http://www.who.int/entity/whr/2003/en/whr03_en.pdf).
- [61] World Health Report, 2004, American Heart Association,  
[http://www.who.int/entity/whr/2004/en/report04\\_en.pdf](http://www.who.int/entity/whr/2004/en/report04_en.pdf).
- [62] Zhou, H. and van Oosterom, A., Application of the boundary element method to the solution of anisotropic electromagnetic problems, *Med Biol Eng Comput.*, Vol. 32(4), pp. 399-405, July 1994.

# APPENDIX 1

## Analytical Derivations for the Homogeneous Torso Model

This section will present the formation of the transformation matrix,  $Z_{BH}$ , that relates the epicardial potentials with the ones of body surface, starting from series of interal derivations and discretization of integrals into matrix forms.

Remembering from Figure 3.1, we have a homogeneous torso model including a volume  $V$  surrounded by heart surface,  $S_H$ , and body surface,  $S_B$ . Barr *et al.* [7] applied Green's second identity to the volume  $V$  and after making corresponding substitutions, received:

$$\int_S \left( \Phi \nabla \left( \frac{1}{r} \right) - \left( \frac{1}{r} \right) \nabla \Phi \right) \cdot \mathbf{n} \cdot dS = \int_V \left( \Phi \nabla^2 \left( \frac{1}{r} \right) - \left( \frac{1}{r} \right) \nabla^2 \Phi \right) \cdot dV, \quad (\text{A1.1})$$

where  $\Phi$  is the scalar electric potential inside the volume  $V$ , and  $1/r$  is the reciprocal of the distance between the observation point  $O$  and the surface of integration, respectively.

In this homogeneous model, and also in reality, there are no current sources exist inside the volume, since the only current generator is heart. Consequently, from Laplace's equation  $\nabla^2 \Phi = 0$  inside the volume  $V$ . Hence, the above equation becomes:

$$\int_S \left( \Phi \nabla \left( \frac{1}{r} \right) - \left( \frac{1}{r} \right) \nabla \Phi \right) \cdot \mathbf{n} \cdot dS = \int_V \Phi \nabla^2 \left( \frac{1}{r} \right) \cdot dV. \quad (\text{A1.2})$$

Additionally, if the observation point  $O$  inside the volume  $V$  is away from the integration surface, then  $\nabla^2 \left( \frac{1}{r} \right) = 0$  for all  $r \neq 0$ .

However, If  $r = 0$ , then we have a singularity because  $\nabla^2 \left( \frac{1}{r} \right)$  is undefined. Here, we use the method in [29, 38] to solve the singularity as follows:

If  $r = 0$ , then the volume integral becomes:

$$-\int_V \Phi \nabla^2 \left( \frac{1}{r} \right) \cdot dV = \Phi(p_S) C, \quad (\text{A1.3})$$

and

$$C = \int_{V_s} \nabla^2 \left( \frac{1}{r} \right) \cdot dV,$$

where  $p_s$  is the point of singularity and  $V_s$  is volume just including the singularity. By divergence theorem, we get:

$$C = \int_{V_s} \nabla^2 \left( \frac{1}{r} \right) \cdot dV = \int_{V_s} \nabla \nabla \left( \frac{1}{r} \right) \cdot dV = \int_{S_s} \nabla \left( \frac{1}{r} \right) \cdot dS. \quad (\text{A1.4})$$

Using spherical coordinates, we get:

$$\lim_{r \rightarrow 0} \int_{S_s} \nabla \left( \frac{1}{r} \right) \cdot dS = \lim_{r \rightarrow 0} 4\pi r^2 \left( -\frac{1}{r^2} \right) \cdot dS = -4\pi. \quad (\text{A1.5})$$

Combining the equations, we end up with the following integral equation:

$$\int_S \left( \Phi \nabla \left( \frac{1}{r} \right) - \left( \frac{1}{r} \right) \nabla \Phi \right) \cdot \mathbf{n} \cdot dS = -4\pi \Phi_o, \quad (\text{A1.6})$$

or in another form:

$$\Phi_o = \frac{1}{4\pi} \int_S \Phi \cdot \frac{\mathbf{r} \cdot \mathbf{n}}{r^2} \cdot dS + \frac{1}{4\pi} \int_S \frac{\nabla \Phi \cdot \mathbf{n}}{r} \cdot dS, \quad (\text{A1.7})$$

where  $\mathbf{r}$  is a unit vector in the direction of  $r$  and  $\Phi_o$  is the potential at point  $O$ . Since, surface  $S$  is composed of two surfaces  $S_H$  and  $S_B$  ( $S = S_H \cup S_B$ ), (A1.7) can be rewritten as a sum of two integral equations, one for the heart surface and the other is body surface:

$$\begin{aligned} \Phi_o = & -\frac{1}{4\pi} \int_{S_H} \Phi_H \cdot \frac{\mathbf{r} \cdot \mathbf{n}_H}{r^2} \cdot dS_H - \frac{1}{4\pi} \int_{S_H} \frac{\nabla \Phi_H \cdot \mathbf{n}_H}{r} \cdot dS_H \\ & + \frac{1}{4\pi} \int_{S_B} \Phi_B \cdot \frac{\mathbf{r} \cdot \mathbf{n}_B}{r^2} \cdot dS_B + \frac{1}{4\pi} \int_{S_B} \frac{\nabla \Phi_B \cdot \mathbf{n}_B}{r} \cdot dS_B. \end{aligned} \quad (\text{A1.8})$$

Note that the minus sign in the first two elements of the equation comes from the reverse direction of the unit normal  $\mathbf{n}_H$  of the inner surface  $S_H$  due to the outer surface  $S_B$ . Finally, utilizing the fact that  $\nabla\Phi = 0$  on the outer surface,  $S_B$ , [38], gives us the following equation:

$$\begin{aligned} \Phi_o = & -\frac{1}{4\pi} \int_{S_H} \Phi_H \cdot \frac{\mathbf{r} \cdot \mathbf{n}_H}{r^2} \cdot dS_H - \frac{1}{4\pi} \int_{S_H} \frac{\nabla\Phi_H \cdot \mathbf{n}_H}{r} \cdot dS_H \\ & + \frac{1}{4\pi} \int_{S_B} \Phi_B \cdot \frac{\mathbf{r} \cdot \mathbf{n}_B}{r^2} \cdot dS_B. \end{aligned} \quad (\text{A1.9})$$

The above analytic equation giving the potential value at an observation point  $O$  in terms of potentials on the heart surface and the ones on the body surface is useful but not applicable, because, evaluating these integrals is not easy. The objective here is to produce a numerical method of finding the potential at a point in terms of heart and body surface potentials.

The approach introduced in [7] allows the observation point to be successively stationed at different locations on either  $S_H$  and  $S_B$ . Suppose that there are  $N_B$  locations on  $S_B$  and  $N_H$  locations on  $S_H$ . Positioning the observation point on the body surface first yields:

$$\Phi_B^i = -\frac{1}{4\pi} \int_{S_H} \Phi_H \cdot d\Omega_{BH}^i - \frac{1}{4\pi} \int_{S_H} \frac{\nabla\Phi_H \cdot \mathbf{n}_H}{r} \cdot dS_H + \frac{1}{4\pi} \int_{S_B} \Phi_B \cdot d\Omega_{BB}^i, \quad (\text{A1.10a})$$

and then on the heart surface yields:

$$\Phi_H^i = -\frac{1}{4\pi} \int_{S_H} \Phi_H \cdot d\Omega_{HH}^i - \frac{1}{4\pi} \int_{S_H} \frac{\nabla\Phi_H \cdot \mathbf{n}_H}{r} \cdot dS_H + \frac{1}{4\pi} \int_{S_B} \Phi_B \cdot d\Omega_{HB}^i, \quad (\text{A1.10b})$$

where

$$d\Omega_{ef}^i = \frac{\mathbf{r}_{ef} \cdot \mathbf{n}_f}{r_{ef}^2} \cdot dS_f.$$

Here,  $i$  is the index of the observation point on the corresponding surface.  $d\Omega_{ef}^i$  is the *solid angle* subtended at an observation point of the  $i$ th location on the surface  $e$  by an area element on surface  $f$ . The computation of the solid angle

is shown in Appendix A.3.

Changing the order of elements in equations (A1.10a) and (A1.10b) results in the following form:

$$-\Phi_B^i + \frac{1}{4\pi} \int_{S_B} \Phi_B \cdot d\Omega_{BB}^i - \frac{1}{4\pi} \int_{S_H} \Phi_H \cdot d\Omega_{BH}^i - \frac{1}{4\pi} \int_{S_H} \frac{\nabla \Phi_H \cdot \mathbf{n}_H}{r} \cdot dS_H = 0, \quad (\text{A1.11a})$$

and

$$-\frac{1}{4\pi} \int_{S_H} \Phi_H \cdot d\Omega_{HH}^i - \Phi_H^i - \frac{1}{4\pi} \int_{S_H} \frac{\nabla \Phi_H \cdot \mathbf{n}_H}{r} \cdot dS_H + \frac{1}{4\pi} \int_{S_B} \Phi_B \cdot d\Omega_{HB}^i = 0. \quad (\text{A1.11b})$$

Each of the terms of (A1.11a) and (A1.11b) can be discretized as follows:

$$-\Phi_B^i + \frac{1}{4\pi} \int_{S_B} \Phi_B \cdot d\Omega_{BB}^i = \sum_{j=1}^{N_B} p_{BB}^{ij} \Phi_B^j, \quad (\text{A1.12a})$$

$$-\frac{1}{4\pi} \int_{S_H} \Phi_H \cdot d\Omega_{BH}^i = \sum_{j=1}^{N_H} p_{BH}^{ij} \Phi_H^j, \quad (\text{A1.12b})$$

$$-\frac{1}{4\pi} \int_{S_H} \frac{\nabla \Phi_H \cdot \mathbf{n}}{r} \cdot dS_H = \sum_{j=1}^{N_H} g_{BH}^{ij} \Gamma_H^j, \quad (\text{A1.12c})$$

$$\frac{1}{4\pi} \int_{S_B} \Phi_B \cdot d\Omega_{HB}^i = \sum_{j=1}^{N_B} p_{HB}^{ij} \Phi_B^j, \quad (\text{A1.12d})$$

$$-\Phi_H^i - \frac{1}{4\pi} \int_{S_H} \Phi_H \cdot d\Omega_{HH}^i = \sum_{j=1}^{N_H} p_{HH}^{ij} \Phi_H^j, \quad (\text{A1.12e})$$

$$-\frac{1}{4\pi} \int_{S_H} \frac{\nabla \Phi_H \cdot \mathbf{n}}{r} \cdot dS_H = \sum_{j=1}^{N_H} g_{HH}^{ij} \Gamma_H^j. \quad (\text{A1.12f})$$

Here,  $\Phi_H$  and  $\Phi_B$  are vectors containing the potentials at the  $N_B$  and  $N_H$  locations on surfaces  $S_B$  and  $S_H$ , respectively, and  $\Gamma_H$  contained the normal components of the gradients of  $S_H$ . The first superscript and first subscript for each of the  $p$ 's and  $g$ 's identifies the location and surface where the observer is stationed. The second superscript and subscript identifies the element of

corresponding surface of integration. The  $p$ 's and  $g$ 's are coefficients whose values are determined on the basis of geometry.

Substituting (A1.12a) - (A1.12f) into (A1.11a) and (A1.11b) yields:

$$\begin{aligned} p_{BB}^i \Phi_B + p_{BH}^i \Phi_H + g_{BH}^i \Gamma_H &= 0, \\ p_{HB}^i \Phi_B + p_{HH}^i \Phi_H + g_{HH}^i \Gamma_H &= 0. \end{aligned} \quad (\text{A1.13})$$

Here,  $i$  denotes the  $i$ th location, first, on surface  $S_B$  and then on  $S_H$ . (A1.13), then, yields (A1.14) by choosing location  $i$  successively at all  $N_B$  locations on  $S_B$ , and on  $N_H$  locations on  $S_H$ :

$$\begin{aligned} P_{BB} \Phi_B + P_{BH} \Phi_H + G_{BH} \Gamma_H &= 0, \\ P_{HB} \Phi_B + P_{HH} \Phi_H + G_{HH} \Gamma_H &= 0. \end{aligned} \quad (\text{A1.14})$$

Here, all  $P$  and  $G$  are coefficient matrices, which are determined from the geometry (see Appendix A.1). These matrices are the ‘‘building stones’’ of the final transformation matrix  $Z_{BH}$ , that relates the potential distribution on the heart surface to the ones on the body surface.

If we solve (A1.14) for  $\Phi_B$  in terms of  $\Phi_H$ , we receive (A1.15):

$$\Phi_B = Z_{BH} \cdot \Phi_H, \quad (\text{A1.15})$$

where

$$Z_{BH} = (P_{BB} - G_{BH} G_{HH}^{-1} P_{HB})^{-1} (G_{BH} G_{HH}^{-1} P_{HH} - P_{BH}).$$

Equation (A1.15) presents that  $Z_{BH}$  is determined from a combination of coefficient matrices which depend only on the geometry.

# APPENDIX 2

## Analytical Derivations for the Inhomogeneous Torso Model

In Appendix A.1, a numerical method of finding a transformation matrix from the geometry of a homogeneous volume conductor taking only heart surface and body surface into consideration and assuming that the conducting medium between these surfaces to be isotropic, has been presented. Based on the assumptions and derivations for a homogeneous volume conductor, in this section, we will introduce a numerical method of finding a transformation matrix that relates epicardial to body surface potentials for an inhomogeneous volume conductor in terms of geometry coefficients and conductivity values.

The model has been extended from a homogeneous volume conductor to one having an isotropic homogeneous lung region. Although, we have two lungs as shown Figure 3.3, these two regions can be treated as one combined region mathematically.

The method of finding a transformation matrix for an inhomogeneous volume conductor is similar to one for the homogeneous case, although, we consider conductivities.

Stanley *et al.* [36] made use of the Green's second identity for the volume  $V$  surrounded by the closed surface  $S$ , which is composed by surfaces of five torso regions (heart, lungs, spine, sternum, body and skeletal muscle layer) and substitute  $A$  with a scalar function  $1/r$  and  $B$  with another scalar function not  $\Phi$ , but  $\sigma\Phi$ , where  $\sigma$  denotes the conductivity of the corresponding region.

If we replace  $\Phi$  in (A1.6) of Appendix A.1 and remember that  $\nabla^2(\sigma\Phi) = 0$ , since, there is no current source in the volume  $V$ , we have the following simplification:

$$\int_S \left( \frac{1}{r} \nabla(\sigma\Phi) - \sigma\Phi \nabla \left( \frac{1}{r} \right) \right) \cdot \mathbf{n} \cdot dS = - \int_V \sigma\Phi \nabla^2 \left( \frac{1}{r} \right) \cdot dV = 4\pi\sigma_o\Phi_o, \quad (\text{A2.1})$$

where  $\Phi_o$  denotes the potential value at an observation point in the volume  $V$ .

Since, surface  $S$  is consisting of three surface  $S_H$ ,  $S_L$  and  $S_B$  ( $S = S_H \cup S_L \cup S_B$ ), (A2.1) can be expanded into a series of integrals considering each surface as the following:

$$\begin{aligned}
& - \int_{S_H} \left( \frac{1}{r_{OH}} \sigma_B \nabla \Phi_H - (\sigma_B - \sigma_H) \Phi_H \nabla \left( \frac{1}{r_{OH}} \right) \right) \cdot \mathbf{n}_H \cdot dS_H \quad (\text{A2.2}) \\
& - \int_{S_L} \left( \frac{1}{r_{OL}} (\sigma_B - \sigma_L) \nabla \Phi_L - (\sigma_B - \sigma_L) \Phi_L \nabla \left( \frac{1}{r_{OL}} \right) \right) \cdot \mathbf{n}_L \cdot dS_L \\
& + \int_{S_B} \left( \frac{1}{r_{OB}} \sigma_B \nabla \Phi_B - (\sigma_{air} - \sigma_B) \Phi_B \nabla \left( \frac{1}{r_{OB}} \right) \right) \cdot \mathbf{n}_B \cdot dS_B \\
& = 4\pi\sigma_o\Phi_o,
\end{aligned}$$

where  $\Phi_H$ ,  $\Phi_L$  and  $\Phi_B$  denotes the potentials on heart, lung and body surfaces, respectively. Similarly,  $\sigma_H$ ,  $\sigma_L$  and  $\sigma_B$  denotes the conductivity values of heart, lung and body surfaces, respectively. Furthermore,  $r_{OH}$ ,  $r_{OL}$  and  $r_{OB}$  denotes the distance  $r$  from an observation point  $O$  to a surface element on the heart, lung and body surfaces, respectively. Finally,  $\mathbf{n}_H$ ,  $\mathbf{n}_L$  and  $\mathbf{n}_B$  denotes the normal vectors of the surfaces  $S_H$ ,  $S_L$  and  $S_B$ .

As a result of the reason that the body is surrounded by air, which is non-conducting ( $\sigma_{air} = 0$ ), the normal component of the current across the body surface is zero:

$$\sigma_B \nabla \Phi_B \cdot \mathbf{n}_B \cdot dS_B = 0.$$

Additionally, at the lung-body boundary, we have the following boundary condition, since, the normal component of the current is continuous:

$$\sigma_L \nabla \Phi_L \cdot \mathbf{n}_L = \sigma_B \nabla \Phi_L \cdot \mathbf{n}_L.$$

We already know that  $\nabla \frac{1}{r} = -\frac{\mathbf{r} \cdot \mathbf{n}}{r^2}$  from Appendix A.2.

Based on the above considerations, we can simplify (A2.2) as follows:

$$\begin{aligned}
\Phi_o &= -\frac{1}{4\pi} \frac{\sigma_B}{\sigma_o} \int_{S_H} \frac{1}{r_{OH}} \nabla \Phi_H \cdot \mathbf{n}_H \cdot dS_H \\
&\quad - \frac{1}{4\pi} \frac{\sigma_B}{\sigma_o} \int_{S_H} \Phi_H d\Omega_{OH} \cdot dS_H \\
&\quad - \frac{1}{4\pi} \frac{(\sigma_B - \sigma_L)}{\sigma_o} \int_{S_L} \Phi_L d\Omega_{OL} \cdot dS_L \\
&\quad + \frac{1}{4\pi} \frac{\sigma_B}{\sigma_o} \int_{S_B} \Phi_B d\Omega_{OB} \cdot dS_B,
\end{aligned} \tag{A2.3}$$

where

$$d\Omega_{ef} = \frac{\mathbf{r}_{ef} \cdot \mathbf{n}_f}{r_{ef}^2}.$$

Here,  $\Phi_o$  is the electrical potential value at an observation point in the volume  $V$ , in terms of the potentials on the heart, lung and body. The notation  $d\Omega_{ef}$  is the solid angle subtended by a surface element  $f$  at an observation point on the surface  $e$ . The computation of the solid angle is represented in the Appendix A.4.

Similar to the approach in the homogeneous case, suppose that there are  $N_H$  locations on surface  $S_H$ ,  $N_L$  locations on surface  $S_L$  and  $N_B$  locations on  $S_B$  and let the observation point to be succesively stationed on  $N_H$ ,  $N_L$  and  $N_B$  locations. After a series of substitutions and discretizations [36], we will receive the following form:

$$\begin{aligned}
P_{BB}\Phi_B + P_{BL}\Phi_L + P_{BH}\Phi_H + G_{BH}\Gamma_H &= 0, \\
P_{HB}\Phi_B + P_{HL}\Phi_L + P_{HH}\Phi_H + G_{HH}\Gamma_H &= 0, \\
P_{LB}\Phi_B + P_{LL}\Phi_L + P_{LH}\Phi_H + G_{LH}\Gamma_H &= 0.
\end{aligned} \tag{A2.4}$$

Here, all  $P$  and  $G$  are coefficient matrices, which are determined from the geometry and conductivities (see Appendix A.2) as in the homogeneous case.

If we solve equation (A2.4) for  $\Phi_B$  in terms of  $\Phi_H$ , we receive equation (A2.5):

$$\Phi_B = Z_{BH} \cdot \Phi_H, \quad (\text{A2.5})$$

where

$$\begin{aligned} Z_{BH} = & ((P_{BB} - G_{BH}G_{HH}^{-1}P_{HB}) \\ & + (P_{BL} - G_{BH}G_{HH}^{-1}P_{HL}) \\ & \cdot (P_{LL} - G_{LH}G_{HH}^{-1}P_{HL})^{-1} \\ & \cdot (G_{LH}G_{HH}^{-1}P_{HB} - P_{LB}))^{-1} \\ & \cdot ((G_{BH}G_{HH}^{-1}P_{HH} - P_{BH}) \\ & + (G_{BH}G_{HH}^{-1}P_{HL}) \\ & \cdot (P_{LL} - G_{LH}G_{HH}^{-1}P_{HL})^{-1} \\ & \cdot (G_{LH}G_{HH}^{-1}P_{HH} - P_{LH})). \end{aligned} \quad (\text{A2.6})$$

Equation (A2.6) presents that  $Z_{BH}$  is determined from a combination of coefficient matrices which depend on the geometry and the conductivities.

# APPENDIX 3

## Calculation of the Solid Angle

The solid angle subtended by a surface at a point is defined as the surface area of the projection of that surface onto a unit sphere centered at that point (Figure 5.1) and usually denoted by  $\Omega$ . The  $P$  matrices defined in previous chapters need the efficient computation of the solid angles.

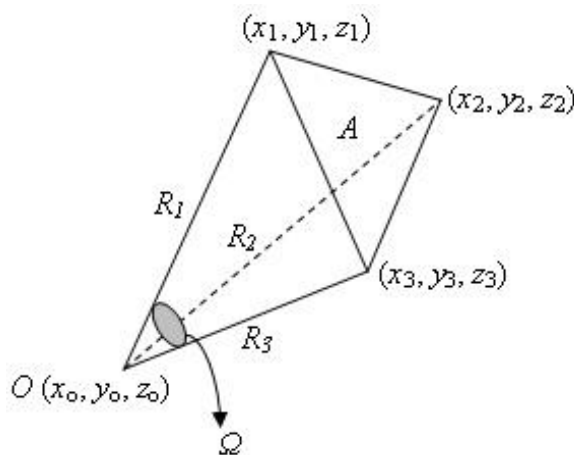


Figure 5.1: Solid angle subtended by a plane triangle at a point.

In Figure 5.1,  $R_1$ ,  $R_2$  and  $R_3$  are three vectors from an observation point  $O$  to the three vertices of a triangle element on the surface of integration,  $A$  is the area of the triangle formed by the end-points of the vectors  $R_1$ ,  $R_2$  and  $R_3$  and  $\Omega$  is the solid angle subtended by surface area  $A$  at observation point  $O$ .

The calculation of the solid angle is one of the main loads in forming transformation matrix [54]. An efficient algorithm for calculating the solid angle  $\Omega$  subtended by a triangle with vertices  $R_1$ ,  $R_2$  and  $R_3$ , as seen from the origin has been given by Oosterom and Strackee [53] in the following equation:

$$\Omega = 2 \arctan \left( \frac{[\mathbf{R}_1 \mathbf{R}_2 \mathbf{R}_3]}{R_1 R_2 R_3 + (\mathbf{R}_1 \cdot \mathbf{R}_2) R_3 + (\mathbf{R}_1 \cdot \mathbf{R}_3) R_2 + (\mathbf{R}_2 \cdot \mathbf{R}_3) R_1} \right). \quad (5.0.1)$$

Here,  $[R_1 R_2 R_3]$  denotes the determinant of the matrix that results when writing the vectors together in a row,  $R_i$  denotes the distance of point  $i$  from the origin,  $\mathbf{R}_i$  is the vector representation of point  $i$ , and  $\mathbf{R}_i \cdot \mathbf{R}_j$  denotes the scalar vector product.

Equation (5.0.1), as the definition implies, is valid when the observation point is at the origin. Because of this, before computing the solid angle, first, the observation point has to be shifted to the origin by subtracting its coordinates  $(x_o, y_o, z_o)$  from the coordinates of each of the vertices of the triangle.

As well as being efficient, this algorithm has limitations on evaluating the solid angle subtended by the triangle at an observation point which is also one of the vertices of the triangle. This condition is named as *auto solid angle*, in which, the denominator in (5.0.1) will be zero and the result of the division operation will be undefined.

The accuracy of the BEM strictly depends on the calculation of solid angles, especially auto solid angles. However, calculation of auto solid angle is singular, as described above, thus, efficient methods [24, 33, 41] are needed.

In the numerical solution given in this study a modified version of the equation (5.0.1) is used with [13] to improve the accuracy of the solution. The solid angles are computed with linear discretization method and the effect of the solid angle is distributed relatively between the nodes of the triangle in consideration, unlike the simple method of Barr [7] in which the effect of the total solid angle was distributed equally to the vertices of the triangle. The auto solid angles, on the other hand, cannot be directly computed with the above equation because of the singularity. Instead, they are computed by subtracting the solid angles computed for the off-diagonal entries of the matrix  $P$  from the total.

# APPENDIX 4

## Integration over a Plane Triangle

The methods presented in this study to form the transformation matrices that relate the epicardial to body surface potentials,  $Z_{BH}$ , consists of evaluating the surface integral  $dS/r$  from an observation point  $O$  distanced  $r$  units to a triangle element  $dS$  (Figure 5.2).

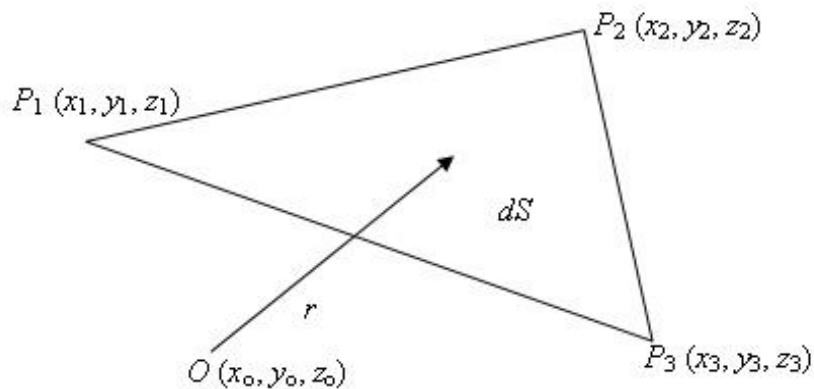


Figure 5.2: Illustration of the integral element  $dS/r$ .

In addition to the calculation of the solid angle, the evaluation of the surface integral  $dS/r$  is one of the main loads in forming transformation matrix. In the simple cases when the observation point  $O$  is not on the integration surface  $S$  or the resultant scalar value, the electrical potential, is assumed to be constant over the integration surface, the integration is relatively simple and may even have a closed analytical solution [7]. The potential value evaluated for the triangle element is then assigned to the vertices of the triangle in some manner, for example, equally in Barr *et al.* [7]. However, in such cases when the observation point is on the integration surface, these integrals become singular – “worst” integrals – , hence, modified techniques are needed to evaluate these integral accurately. Because of the reason that these “worst” integrals are in general the largest in magnitude and lead to the diagonally dominant matrix equation and

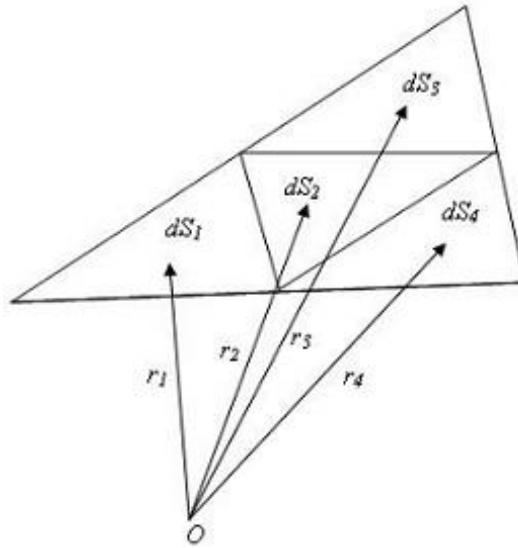


Figure 5.3: Adaptive numerical algorithm for evaluating surface integration [23].

have most influence on the solution, it is important to calculate these integrals as accurately as possible [26] by using modified integration techniques.

A modified approach in which each original planar element is subdivided and a constant value is assigned to each of the resulting subelements has been introduced by [23]. The specifics of this technique depend on exactly how the triangle is subdivided (Figure 5.3), and how potentials are assigned to the resulting subelements. One important advantage of this method is that it permits adaptive solutions in which subdivision occurs only where and when required, resulting in increased computational efficiency.

A good approximation for the previous approach has been given by Oostendorp and van Oosterom [35]. Instead of using the computation time consuming analytical expressions for the calculation of the integral  $1/r$ , the mean of the values of  $1/r$  at the vertexes of the triangle is multiplied by the area of the subtriangle. Similar to the auto solid angle case mentioned in Appendix A.4, a singularity arises here when  $r$  is 0, in other words, when the observation point is one of the vertexes of the triangle. By an approximation, this singularity is solved by taking the value of  $1/r$  at the center of mass of the subtriangle instead of infinite value at the observation point. The same approach was utilized in

[49], where, the area integral was estimated as the area of each triangle divided by the distance from the observation point on the scalp to the centroid of each triangle. The potential was assumed constant over each triangle and equal to the average potential over the three vertices (nodes) of the triangle.

A third approach to approximating the integrals in boundary elements is to allow the scalar value to vary over the surface element and then employ numerical surface integration (numerical quadrature) techniques based on Radon [40] for each element [11, 30, 36]. The numerical quadrature then becomes a weighted average of the potentials at the vertices.

De Munck [13] presented more general choices to discretize the boundary integral equations, without destroying the analytical computation of the matrix elements. The later study [46] implemented the approach presented by de Munck in calculating the electric potential and investigating the effect of different discretization choices.

The surface integrations evaluated in this study are based on De Munck's approach with modifications by Ferguson et al. [15].

In BEM, as well as the computation of the surface integral is important, one should take attention on the discretization of the surfaces. If there is a large number of points and triangles (i.e., hundreds, thousands) in the model, then the numerical errors in computing surface integrals and solid angles may be decreased. However, this increase in the number of discretization points will result in extensive computation time and storage demands [33]. As a result, in order to receive reasonable results from BEM, special care is needed for computing surface integrals and solid angles.

# APPENDIX 5

## Inverse Problems

Aster *et al.* [4] defined a system as a composition of physical parameters and observations. Scientists and engineers frequently need to relate the physical parameters to observations of the system. Mathematically, a system can be represented as:

$$G(m) = d, \tag{A5.1}$$

where  $m$  refers to physical parameters or model,  $d$  refers to observations or data and  $G$  is a function or forward operator that relates the model  $m$  to data  $d$ .

In applied mathematics,  $G(m) = d$  usually refers to the “mathematical model”, and  $m$  refers to the “parameters” of the mathematical model.

The data  $d$  may be a continuous function of time and space, or may be a collection of discrete observations. In addition, the model  $m$  may be a continuous function of time and/or space, or it may be a collection of discrete parameters as well. The operator  $G$  can take on many forms. In some cases,  $G$  is an ordinary differential equation (ODE) or partial differential equation (PDE). In other cases,  $G$  might be a linear or nonlinear system of algebraic equations.

The data has two important issues. One of them is that the actual observations always contain some amount of *noise* which may arise due to missing specifications in the model or numerical errors. The second issue is that there are also commonly an infinite number of models that satisfy the data  $d$ , for the same  $G$ . The forward problem is to find  $d$  given  $m$  by computing  $G(m)$ , which might involve solving an ODE, solving a PDE, evaluating an integral, or applying an iterative or adaptive algorithm. The inverse problem, on the other hand, is to obtain an estimate of  $m$  given  $d$ .

In the cases, where  $m$  and  $d$  are characterized as continuous functions of time and space, associated task of estimating  $m$  from  $d$  is called a *continuous inverse problem*.

However, in many cases, we will want to determine a finite number, of param-

eters,  $n$ , that define a model  $m$ . Then, we can express  $m$  as a vector of  $n$  parameters. Similarly, the data  $d$  can be expressed an  $m$ -dimensioned vector  $d$ . Such problems are called *discrete inverse problems* or *parameter estimation problems*. A general discrete inverse problem can be written as a (possibly nonlinear) system of equations:

$$G(\mathbf{m}) = \mathbf{d}, \tag{A5.2a}$$

or

$$G \cdot \mathbf{m} = \mathbf{d}. \tag{A5.2b}$$

Solving a forward problem is easy and straightforward; since, for a specific model  $m$  and a forward operator  $G$ , computing the data  $d$  is obvious. Unlike the forward problem solving an inverse problem, in other words finding mathematically acceptable answers to inverse problems, is hard. Because, there may be many models that adequately fit the data. In order to decide whether the solution is acceptable or not, some important issues that must be considered include *existence*, *uniqueness*, and *instability* of the solution.

1. *Existence*: There may be no model  $m$  that exactly fits a given data  $d$ .
2. *Uniqueness*: If exact solutions do exist, they may not be unique, even for an infinite number of exact data  $d$ .

For example, let  $m_1$  and  $m_2$  be two solutions of the inverse problem that  $m_1 \neq m_2$ , then the following two equation can be acceptable due to the same data  $d$ :

$$G \cdot m_1 = d,$$

and

$$G \cdot m_2 = d.$$

3. *Instability*: The process of computing an inverse solution is often extremely unstable. That is, a small change in measurement can result an

enormous change in the inferred model. Systems where small changes in the data can drive large changes in inferred models are referred to as *ill-posed* (in the case of continuous systems), or *discrete ill-posed* or *ill-conditioned* (in the case of discrete linear systems).

Ill-conditioning of the problem arises from the situation that the operator  $G$  (it is a matrix in discrete inverse problem) is sparse and has a large condition number, singular values of  $G$  decay gradually to zero or the ratio between the largest and smallest nonzero singular values is large.

An interesting and important aspect of ill-posedness is that the ill-conditioning of the problem does not mean that a meaningful approximate solution cannot be computed, however, means that the standard methods such as LU decomposition, Cholesky or QR factorization cannot be used in a straightforward manner. Instead of these numerical methods, more sophisticated ones - regularization methods (Tikhonov regularization, quadratic least squares, singular value decomposition) - must be applied to ensure the computation of a meaningful solution [22]. Additionally, some *preconditioning* methods [34, 48, 52, 1] should be used to make the problem well-conditioned by decreasing the condition number of the sparse matrix  $G$ , because computing with a sparse matrix needs so much time and memory space.